





## Article

# Appraising the Seismic Response of a Retrofitted Adobe Historic Structure, the Role of Modal Updating and Advanced Computations

Seyed Salar Ahmadi <sup>1</sup>, Georgios Karanikoloudis <sup>1,\*</sup>, Nuno Mendes <sup>1</sup>, Rogiros Illambas <sup>1</sup>  
and Paulo B. Lourenço <sup>1</sup>

ISISE, Department of Civil Engineering, University of Minho, 4800-058 Guimarães, Portugal

\* Correspondence: id5702@alunos.uminho.pt; Tel.: +351-912258827

**Abstract:** The concepts of structural assessment and retrofit of historical constructions are of particular complexity and require advanced knowledge in material science, conservation techniques and structural analysis. In particular, adobe constructions, given their low mechanical properties and brittle failure modes, are in immense need of comprehensive assessment and retrofitting plans. The current work focuses on the adobe Church of Kuñotambo in Peru, having experienced long periods of deterioration and earthquake-related damage. Under the ongoing Seismic Retrofitting Project (SRP) of the Getty Conservation Institute (GCI), the structural assessment of the church initiated in 2015 confirmed the low lateral capacity of the building and the poor connectivity between the structural parts. Based on the existing cracks and damage, a strengthening scheme was optimized and validated. After the implementation of the retrofitting plan, the quality of its execution and efficiency were assessed in 2019 with a new in situ campaign, which included ambient vibration testing (AVT) and sonic testing. From the acquired field data, the FE model of the retrofitted church was optimized, by updating the stiffness properties of masonry and discontinuities. Moreover, nonlinear static analyses were performed on the updated model in all in-plan directions. Finally, a displacement-based performance assessment was undertaken, under different earthquake limit states, demonstrating the adequacy of the retrofitting.

**Keywords:** adobe church; strengthening of historical constructions; in situ survey; non-destructive test campaign; FE modeling; modal updating; static nonlinear analysis; performance-based seismic assessment



**Citation:** Ahmadi, S.S.; Karanikoloudis, G.; Mendes, N.; Illambas, R.; Lourenço, P.B. Appraising the Seismic Response of a Retrofitted Adobe Historic Structure, the Role of Modal Updating and Advanced Computations. *Buildings* **2022**, *12*, 1795. <https://doi.org/10.3390/buildings12111795>

Academic Editor: Luca Pelà

Received: 6 September 2022

Accepted: 28 September 2022

Published: 26 October 2022

**Publisher's Note:** MDPI stays neutral with regard to jurisdictional claims in published maps and institutional affiliations.



**Copyright:** © 2022 by the authors. Licensee MDPI, Basel, Switzerland. This article is an open access article distributed under the terms and conditions of the Creative Commons Attribution (CC BY) license (<https://creativecommons.org/licenses/by/4.0/>).

## 1. Introduction

Adobe constructions account for a significant portion of the international built heritage. Important adobe monuments range from archaeological sites that date from as early as the Neolithic era (e.g., Tukestan, Assyria) [1] to tower-like structures (Shibam in Yemen) built 500 years ago [2]. Although adobes are nowadays mostly used in rehabilitation projects in developed countries, the material is still much-used for auto-construction in many developing countries. In addition, efforts are currently being made around the world to use adobes in contemporary sustainable architecture [3].

Adobe masonry structures are considered to be quite vulnerable to earthquake actions. Poor seismic performance is mostly due to high inertia forces, and the low strength and brittleness of the material. Structural response is often affected by inadequate interlocking among walls and the absence of bracing and diaphragmatic strengthening elements. The inability of the structure to develop “box behavior” during earthquakes typically leads to in-plane diagonal cracks, horizontal cracks at the base, vertical shear cracks at intersections, disintegration of material at compression zones, separation and overturning of walls, and corner dislocations [4]. The overall behavior is influenced by the physico-chemical characteristics of the material itself. Adhesion between the adobes and the mud jointing

mortar is generally weak [5]. This is sometimes worsened by poor interparticle chemical bonding due to low clay content in the materials' composition. Adobe masonry generally exhibits rather low mechanical properties [5]. Compressive strength in air dry conditions varies from 1–3 MPa for adobe units and from 0.5–3 MPa for the masonry. Young's modulus of the masonry is usually <1 GPa and can even reach a lower bound of 100 MPa [5].

Seismic vulnerability of adobe structures is verified by the fact that the 1966 strong earthquakes that occurred between 1900 and 2011 caused heavy damage to earthen and rubble masonry constructions, resulting in approximately 38% of the casualties due to natural disasters [6]. Peru is among the countries that suffered important social and economic losses, with significant damage to adobe constructions being recorded in the 1970, 1996, 2001 and 2007 earthquakes [7]. In fact, the 2007 Pisco earthquakes in Central Peru were responsible for severe damage to 80% of the adobe building stock, and the total collapse of 32% of the historic and monumental structures, in the Pisco area [7,8].

In general, retrofitting schemes in masonry buildings at seismic prone areas, often involve bracing elements, embedded or in the circumference, either in timber or metallic, accounting for an increase in diaphragmatic stiffness and connectivity between parts, as demonstrated in [9–12]. The current study, which is a component of the Seismic Retrofitting Project (SRP) of the Getty Conservation Institute (GCI), examines the structural performance of the retrofitted Church of Kuñotambo in Peru. This historic monument was strengthened using traditional techniques that include the addition of timber elements (bond beams, tie beams, anchors and corner keys), the construction of new adobe buttresses and the partial replacement of damaged and deteriorated masonry units. An integrated methodology for the quantitative appraisal of the retrofitting scheme is hereby presented. Assessment is based on FE analyses of 3D continuum macro-models, while local discontinuities (cracks, weak connections), detected following in situ testing, are accounted for. This paper demonstrates through the selected case study the process of developing and calibrating a numerical assessment model using experimental methods (including non-destructive tests) and physical observations. It also addresses the nonlinear pushover analysis of masonry structures, considering a translational single-degree-of-freedom transformation method and examining different criteria for the determination of the displacement capacity. The proposed approach is considered to be a major contribution to the literature which, despite the significant advances observed in the field of historic masonry structural analysis, still lacks adequate guidance, regarding the adaptation of procedures developed for engineered constructions, in the case of non-engineered earthen buildings.

## 2. Description of the Structure and Retrofitting Scheme

### 2.1. The Church of Kuñotambo

The Iglesia de Santiago Apóstol, the “Kuñotambo Church”, dates from the 17th century and belongs to the Comunidad Campesina Kuñotambo, a rural hamlet of 500 inhabitants located southeast of Cusco in the province of Acomayo, in the Peruvian Andes. The church (Figure 1) is a one-story masonry structure constructed in the traditional Andean village church style. It comprises an elongated nave which is rectangular in plan and accommodates a choir loft on its east side and a presbytery and an altar on its west side. A baptistery and a sacristy are attached to the east and west ends of the nave's north wall [13].

The walls of the Kuñotambo Church, like the rest of the town, are made of adobe blocks jointed with mud mortar [13]. Rubble stone masonry, with mud mortar, is used to build a base course plinth, over a sloped substrate. The base course changes in height in accordance with the natural slope of the terrain, ranging between 1.20 and 1.50 m, with a maximum height of 3.5 m in the northeast corner of the baptistery [4]. The thickness of the main lateral walls varies between 1.60 and 1.90 m, while the wall thickness of the baptistery ranges between 0.60 and 2.00 m, with the presence of niches and the internal staircase [4]. The height of the walls from the defined-as-zero level (Figure 1) reaches 6.6 m for the nave, presbytery and altar, with the gable end of the east (main) façade reaching a height of 8.7 m. The side walls of the baptistery and sacristy reach the maximum height of 3.8 m and 3.6 m,

respectively, while their gable ends are 5.7 m and 5.5 m high, respectively [4]. The main walls of the nave, presbytery and altar are covered with earthen plaster, and decorated with paintings in the interior [6]. The floor is covered with clay tiles and two wooden pilasters support the timber choir loft [6].

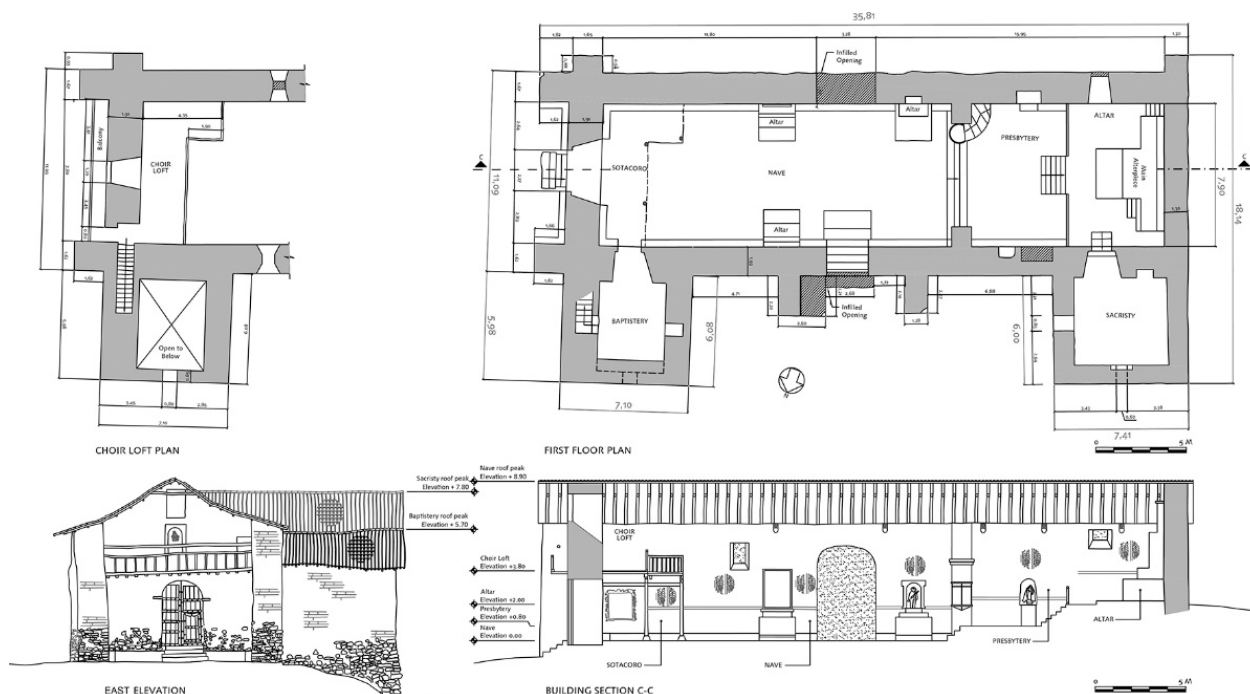


**Figure 1.** The Church of Kuñotambo: plans at choir loft level and at base floor level, east façade and longitudinal section at nave, presbytery and altar, from 2015, before retrofit [13].

## 2.2. Strengthening Process

The design of the retrofitting scheme for the Kuñotambo Church aimed to increase the structure's capacity to comply with a seismic peak ground acceleration of 0.25 g [14], using only traditional techniques. Interventions included buttressing to increase the out-of-plane capacity of walls, reconstructions and architectural modifications to restore the functionality of structural components, and the installation of timber elements (bond beams—wall plates, anchored ties and corner keys) to strengthen the connections among walls, improving the resistance against lateral forces [6,7,9,15].

### 2.2.1. Architectural Modifications and Structural Additions

Three buttresses were added to the south lateral wall of the nave to increase its out-of-plane capacity (Figure 2). Their number and thickness were verified with kinematic analyses. Connectivity between the new buttresses and the existing wall was established by means of interlocking adobe blocks and horizontal timber keys. Highly damaged masonry parts were reconstructed using new adobe and stone blocks. The collapsed semicircular *quincha* arch (*quincha* is a traditional construction system comprised of wood framing covered with mud), separating the nave from the presbytery and altar, was rebuilt (Figure 3a). It is noted that this component was not considered to contribute to the global structural behavior and was excluded from the analysis. The sections of the lateral walls west of the *quincha* arch were elevated by 0.65 m, by adding further adobe courses (Figure 2).

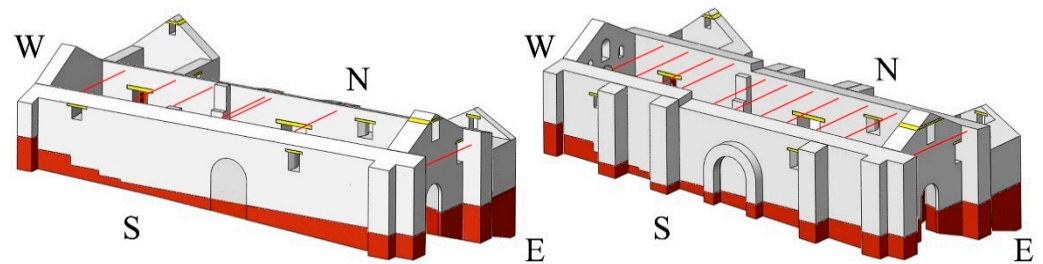


**Figure 2.** Three-dimensional model of the Church of Kuñotambo before (left) and after (right) strengthening.

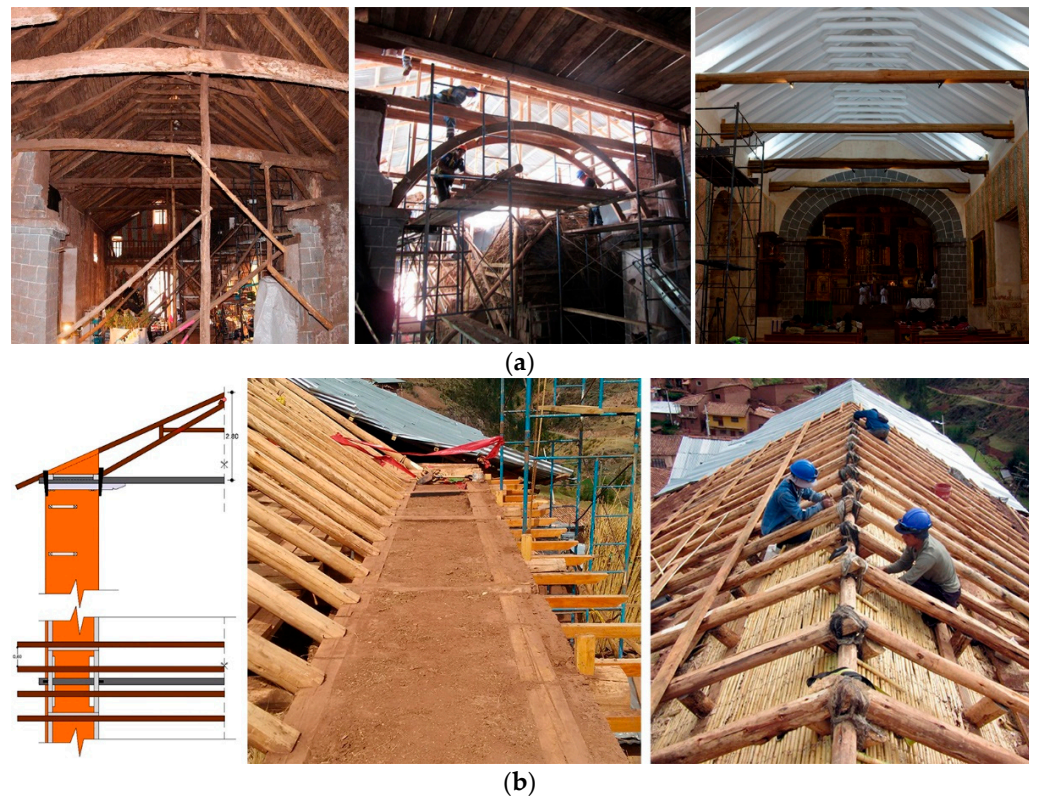


**Figure 3.** (a) Reconstruction of *quincha* arch; (b) Double rafter roof configuration. Note the anchor keys of the tie beam system, in the exterior and interior wall surfaces, highlighted in black.

The roof structure was deemed inadequate in terms of local connections and stiffness. It was also found to be severely deteriorated, while some parts had collapsed. As a result, the existing roof was replaced by a new one. The latter was composed of double rafter timber trusses resting on top of wall plates and joined with a collar tie beam, and with a ridge beam on the top, as shown in Figure 3b. Trusses have a spacing of 0.60 m. The external rafter was extended by approximately 1.0 m over the junction with the outer wall plate, thus producing an overhang to protect the structure from rainwater.

### 2.2.2. Orthogonal Corner and Horizontal Buttress Timber Keys

Orthogonal timber keys were placed in different elevations to improve the connection at corner junctions. The keys were extended to cross cracks, close to the corners, with suitable bearing length, considering the observed damage and the crack development predicted from structural analyses. Keys are situated at elevation planes of approximately 1.0 m and 2.5 m from the top wall elevation (external edge), as illustrated in Figure 4. The corner keys are configured with two sets of timber beams with a maximum distance between axes of 0.6 m, connected transversally with timber blockers, with a maximum

spacing of 1.5 m. Keys are embedded in the exterior part of the adobe walls. All timber elements are  $4 \times 4$  sq. in. ( $10 \times 10$  cm<sup>2</sup>) in cross-section, with half-lapped and pinned connections and leather straps.



**Figure 4.** Configuration of timber-embedded corner keys and horizontal buttress timber keys in elevation. Several views are shown during the retrofitting work, with the timber-embedded elements highlighted in red.

Horizontal timber keys were also inserted along the interfaces between the existing and new buttresses and the adjoining walls, as presented in Figure 4. Their cross-section is chosen to be  $6 \times 6$  sq. in. ( $15 \times 15$  cm<sup>2</sup>).

### 2.2.3. Tie Beams and Bond Beams

A timber bracing system was installed on top of the lateral walls. The tie beams provide lateral restraint, primarily to the weak north and south lateral walls. The anchoring system allows ties to work in tension and compression in the event of an earthquake, with vertical timber anchors in the interior and exterior surfaces (Figure 3b). The anchors are wedged into holes drilled in the tie beams. Their upper section measures  $3 \times 6$  sq. in. ( $7.5 \times 15$  cm<sup>2</sup>), while the lower section measures  $3 \times 3$  sq. in. ( $7.5 \times 7.5$  cm<sup>2</sup>). The exterior and interior anchors are 0.80 and 0.90 m long, respectively.

New tie beams cover the entire thickness of the lateral walls and are laid upon timber corbels. With a bearing length of at least 20 cm, the new anchors penetrate the tie beam and corbel sections. A system of 12 tie beams of 8 × 8 sq. in. (20 × 20 cm<sup>2</sup>), in section, is implemented for the nave presbytery and altar, plus two beams, enclosed within the *quincha* arch. For the baptistery and sacristy, two tie beams are added. The system is supported by rectangular wall plates with a section of 1 × 8 sq. in. (2.5 × 20 cm<sup>2</sup>) and a length of 1.20 m, distributing vertical loads to the lower courses of adobe masonry.

An embedded timber frame, which serves as a bond beam, is implemented over the tie beams. The frame consists of paired longitudinal beams 6 × 6 sq. in. (15 × 15 cm<sup>2</sup>), in section, located close to the boundary edges of the walls and connected to the tie beams. Timber blockers of the same cross-section are set with a maximum spacing of 1.50 m. The configuration of tie beams and bond beams is shown in Figure 5a. The bond beams serve as the supporting base for the roof timber rafters. In order to achieve a continuation of the bond beams of the nave with the elevated presbytery, a timber box with four timber posts of the same cross-section was added, as shown in Figure 5b. The timber system, with the tie beams, vertical timber anchors and connection with the timber roof rafters, is presented in Figure 6. Full details of the timber skeleton can be found in [16].

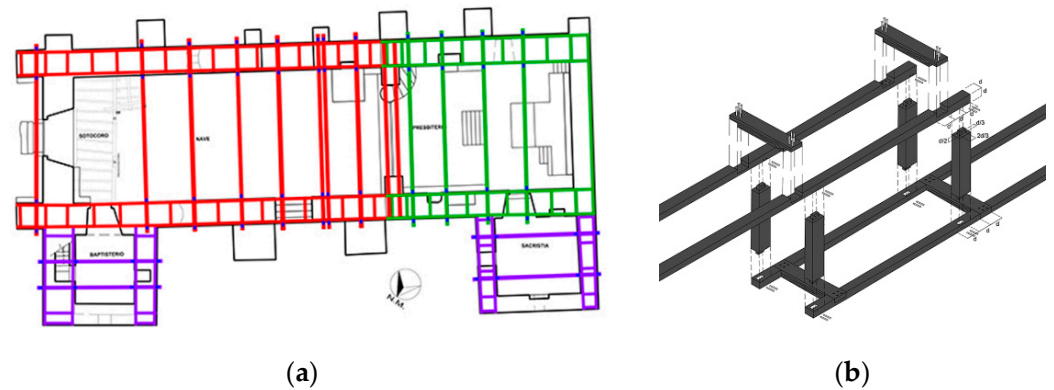


**Figure 5.** Configuration of the tie beams–bond beams system (a) and details of the timber box in the transition of the nave, presbytery and altar lateral walls (b).

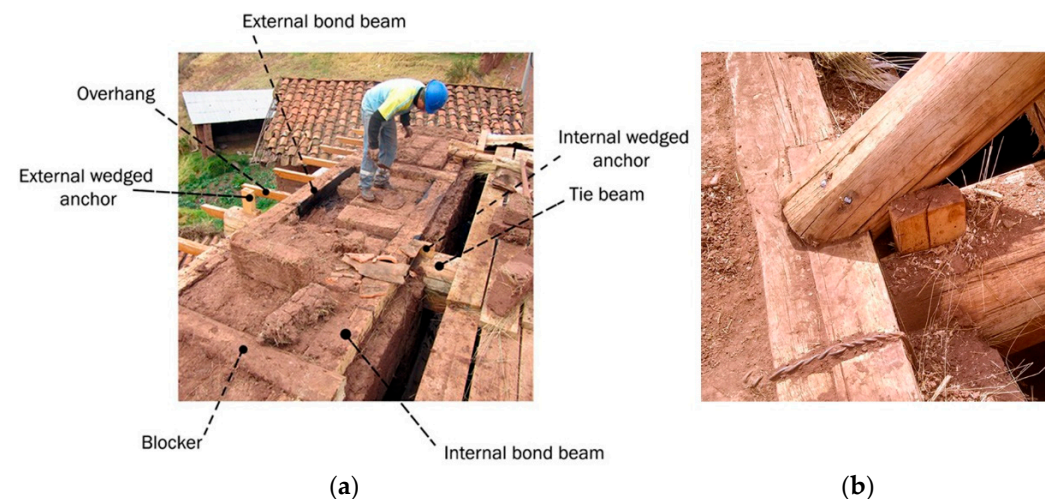


**Figure 6.** Implementation of the retrofitting plan in the Church of Kuñotambo: (a) configuration of tie beams–bond beam system at the southwest corner of the altar; (b) close view of the system of wall plates and tie beam, in connection with the inner part of the new roof rafters.

### 3. In Situ Inspection and Non-Destructive Testing Campaign after Strengthening

#### 3.1. Condition Mapping

The condition mapping of the retrofitted Church of Kuñotambo was conducted through visual inspections, in December 2019, soon after the completion of the restoration works. The damage detected mostly involved cracking at the intersections between structural elements and at the intrados of the roof, and early-stage deterioration due to insufficient drainage (Figures 7–9).

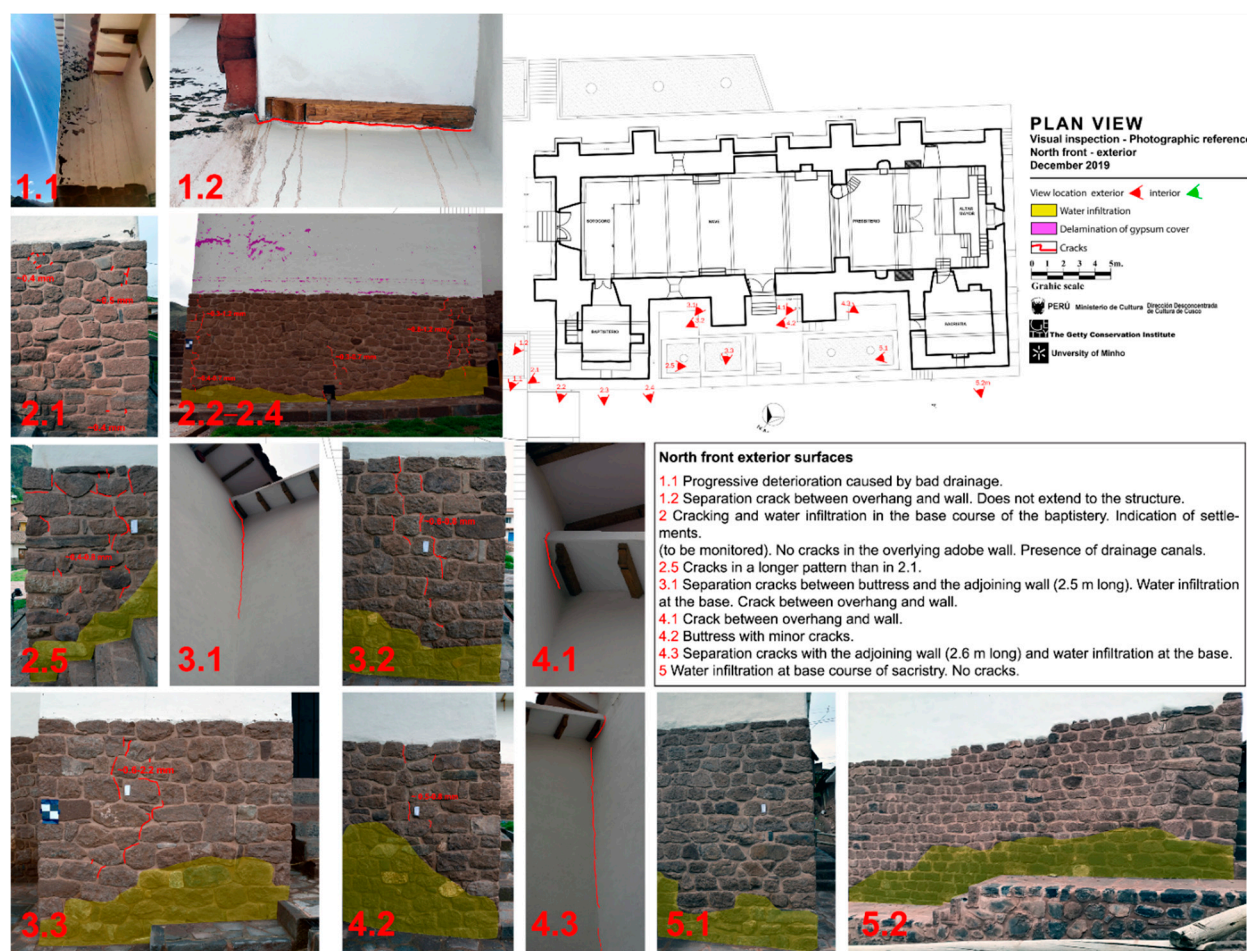


**Figure 7.** Set of documented damages comprised at the exterior surfaces of the south elevation. Note the photo references.

On the east façade, narrow cracks were present at the intersection between the gable wall and the nave (11.1 in Figure 8). These cracks indicate poor interlocking of the walls and out-of-plane deflections due to the flexible roof diaphragm. Narrow cracks were also present on the interior surfaces of the gable end (19.1–19.4 in Figure 9) and near the abutments of some roof rafters (11.2 in Figure 8). Such cracks may have been triggered by thermal variations, wind actions, small earthquakes or wet–dry cycling of adobe masonry.

Signs of inadequate drainage were found (1.1–1.2 in Figure 7). Due to deficient roof waterproofing, rainwater ingress was observed in the staircase leading to the choir loft (15.3 in Figure 9). Moisture-driven damage was also observed along the base of the north façade (2.2–2.5, 3.2–3.3, 4.2 and 5.1–5.2 in Figure 7). This is possibly due to the action of wind-driven rain, in combination with the capillary rise of ground water and condensation.

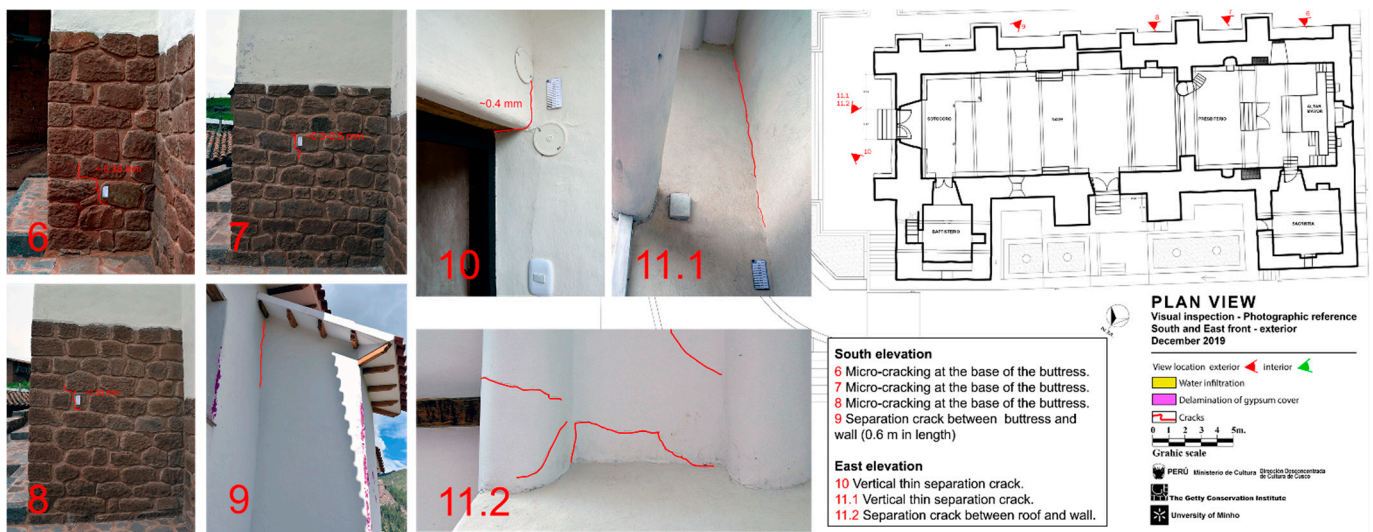


**Figure 8.** Set of documented damages comprised of thin cracks, at wall intersections and the base course of the new buttresses. Note the photo references in the plan view.

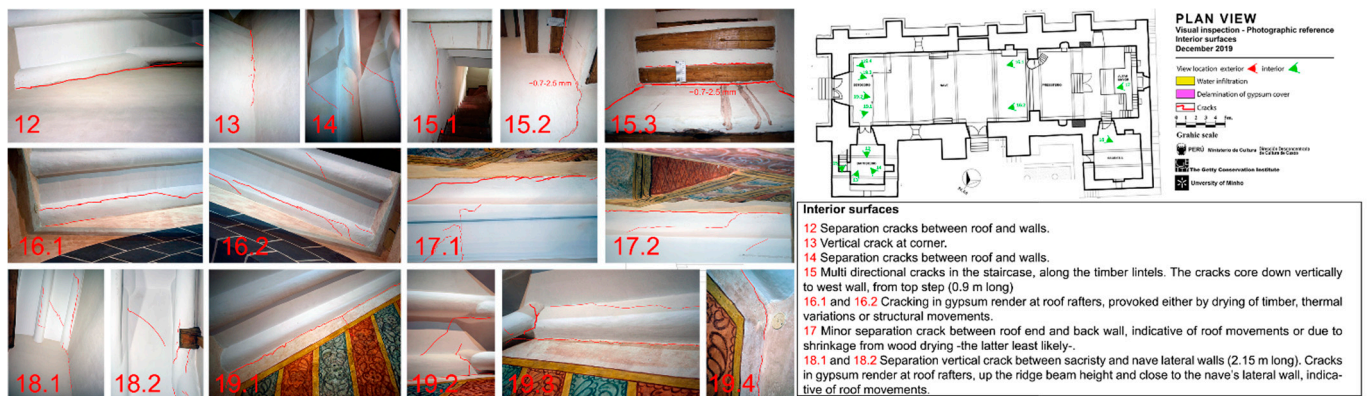


**Figure 9.** Set of documented damages comprised of thin cracks, at wall intersections, and for the roof's gypsum finishing in the interior surfaces. Note the photo references in the plan view.

Vertical cracks (medium to wide, with a thickness of 0.3–1.2 mm) were noted at the stone plinth on both corners of the baptistry (2.1–2.5 in Figure 7). These indicate the separation of the reconstructed exterior leaf of the stone masonry which has weak interlocking with the existing wall's core. Damage can be associated with cracking at the staircase compartment (15.1–15.3 in Figure 9) and may be related to differential settlements.

Cracks were also identified at the top of the buttresses (3.1, 4.1 and 4.3 in Figures 7 and 9 in Figure 8). These were narrow continuous cracks, 0.6–2.6 m long, that ran vertically along one corner of the buttresses at the interface with the adjoining lateral nave walls. Moreover, the horizontal interface with the overhang appeared cracked.

Regarding the condition of the new roof system, several cracks were identified at the interface between the roof and the gable ends, and at the transition with the *quincha* arch (16.1–16.2 in Figure 9). Similar cracks were identified in the interfaces of the roof at the baptistry and sacristy (12–14 and 18.1–18.2 in Figure 7).

### 3.2. Ambient Vibration Tests

The University of Minho conducted ambient vibration tests (AVT) in the retrofitted church in December 2019, to determine its natural frequencies, mode shapes and damping ratios. The aim was to assess the dynamic properties of the structure in order to allow structural health monitoring (SHM) to facilitate the development and validation of nu-



merical models [17,18]. An AVT study of the un-retrofitted church [4] showed that the dynamic behavior was influenced by weak connectivity at the corners of the central nave and by inactive tie beams. The main modes for the lateral nave walls were configured in out-of-plane bending and ranged from 1.6 to 2.7 Hz [4].

The AVT of the retrofitted church was comprised of four setups, as shown in Figure 10. The sensors used were piezoelectric mono-axial accelerometers with a frequency range of 0.15 to 1000 Hz, a measurement range of  $\pm 0.5$  g and a sensitivity of 10,000 mV/g, while the sampling frequency was set at 200 Hz. The top parts of the lateral walls of the nave and the gable ends of the north and south façades, as well as the gable walls of the baptistery and sacristy, were chosen as monitoring points (referenced as  $ACC_{i,j}$ , where  $i$  is the setup number and  $j$  is the accelerometer number). Except for one in-plane monitoring point, all the rest were out-of-plane, with sensors mounted in locations based on accessibility (Figure 10). The position of the reference accelerometer ( $ACC_{i,1}$  in Figure 10) was chosen in the out-of-plane direction of the south lateral wall, at the middle of the nave, similar to the AVT of the un-retrofitted state.

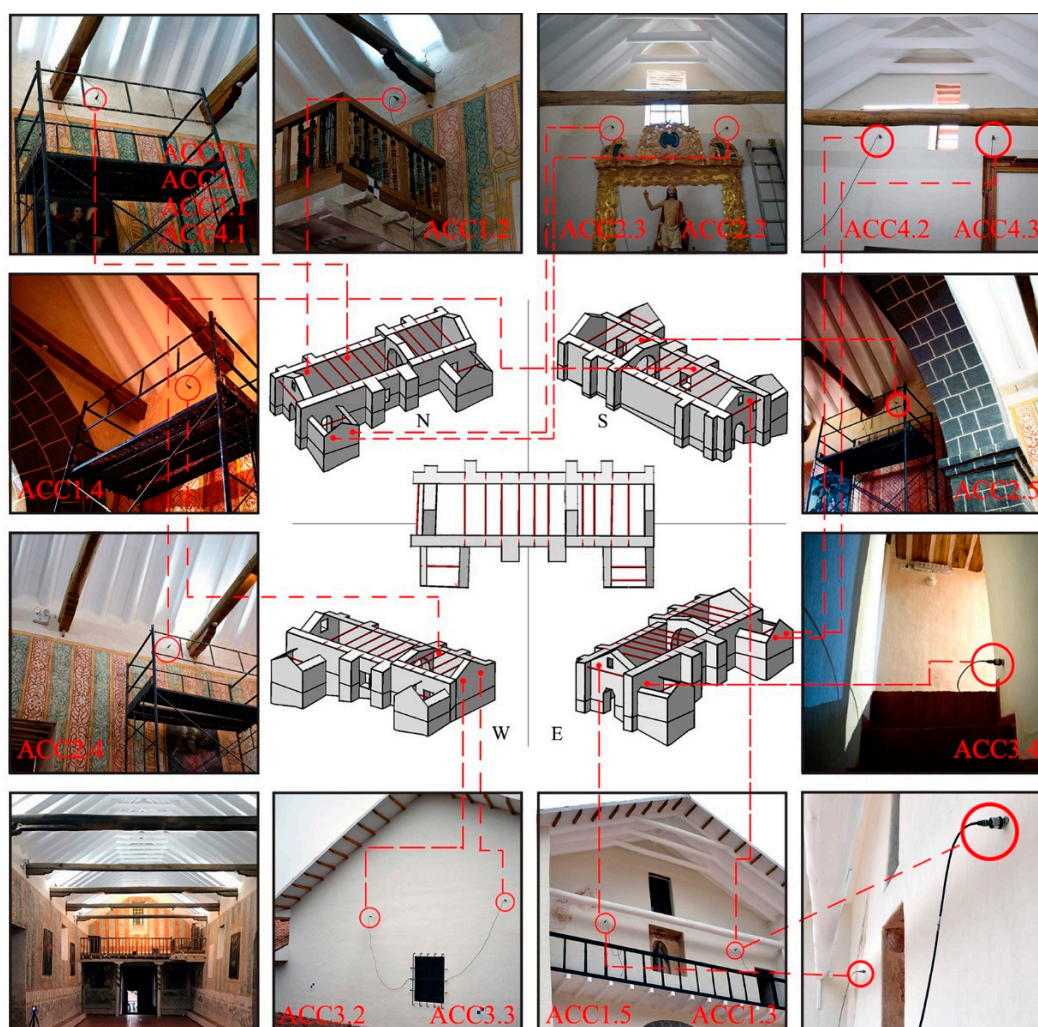


**Figure 10.** Dynamic identification tests in the retrofitted Church of Kuñotambo: placement of accelerometers at the nave, presbytery, altar, baptistery and sacristy gable walls.

The processing of acceleration time histories was performed by the ARTeMIS software, in which the Stochastic Subspace Identification (SSI) method, namely the Unweighted Principal Components (UPC) method and the Enhanced Frequency Decomposition Domain (EFDD) method, was used [19]. Because the EFDD method has difficulty recognizing

frequency peak values, especially in higher modes, the mode shapes obtained from the SSI-UPCX method were tentatively assigned as the modal parameters for the retrofitted state, as shown in Figure 11. Here, the frequencies and damping ratios of the identified modes range between 2.04 Hz and 17.20 Hz and between 0.68% and 4.19%, respectively.

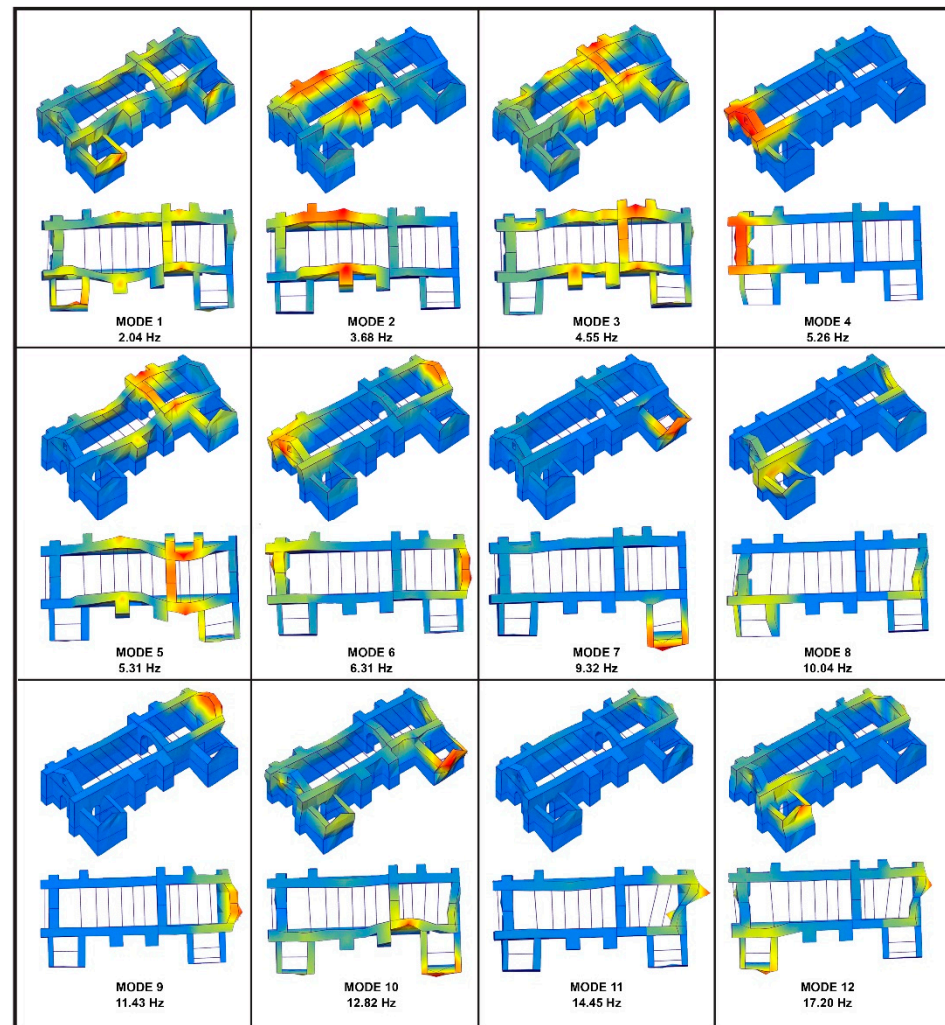


**Figure 11.** Mode shapes obtained from the SSI-UPCX method, of twelve identified modes with linear interpolation, within three surrounding nodes.

The retrofitted structure exhibits a more global behavior compared to the un-retrofitted state. The improved connectivity in the corners, the anchoring of the tie beams and the addition of a bond beam and timber keys resulted in higher stiffness and an integral response. The retrofitted structure presents in-phase bending modes of single curvature, in this case, Mode 2 (3.68 Hz) and Mode 3 (4.55 Hz). Mode 1, estimated at 2.04 Hz, is a complex out-of-plane bending mode of third-order curvature, which involves mostly the nave and presbytery. Yet, from the power spectral density graphs, the peak is quite steep and with low energy. There is a chance that it is a mode generated by the flexible roof, or that the mode is an artefact and does not represent the reality. Mode 3 (4.55 Hz) involves the walls of the presbytery, which appear to be stiffer than those of the nave after the reconstruction of the *quincha* arch and the asymmetrical addition of new buttresses on the south façade.

### 3.3. Sonic Tests

For the retrofitted church, an extensive sonic testing campaign was undertaken in December 2019 to evaluate the dynamic Young's moduli ( $E_{\text{dyn}}$ ) of the materials [20]. It is noted that analogous tests were conducted on the un-retrofitted structure in May 2015 [4]. Two uniaxial accelerometers with a high resolution ( $0.0008 \text{ m/s}^2$ ), a sensitivity of  $1000 \text{ mV/g}$  and a frequency range of  $2\text{--}10,000 \text{ Hz}$  (5%) were used as receivers for the impulsive signals during the sonic tests. A modally tuned impulse hammer with a force sensor, a variety of tips, a sensitivity of  $11.2 \text{ mV/N}$  (15%), a hammer mass of  $0.1 \text{ kg}$  and a measurement range of  $444 \text{ N pk}$  was used as the pulse generator. The LabVIEW Sonic Analyzer 8.5 software was used to calculate the time of arrival and velocity of each impulse wave as well as the distance between emission and reception.

Table 1 compares the results of sonic tests before and after the retrofitting scheme. The  $E_{\text{dyn}}$  obtained from indirect sonic measurements on the rubble stone masonry base of the baptistery (test code IB-) remained unaltered after reconstruction of this section's exterior leaf, i.e.,  $1.6 \text{ GPa}$ . Direct sonic tests performed at the base course of the north and south walls' buttresses gave much lower results, as the inner rubble core was considered in these measurements. The  $E_{\text{dyn}}$  determined at the base of the north buttress (Figure 12) is  $450 \text{ MPa}$  (NB/DB-1), while that of the buttress added on the south wall was  $720 \text{ MPa}$ . The higher modulus of the newly constructed buttress is possibly due to the more regular construction pattern adopted.

**Table 1.** Results for the sonic tests in the Church of Kuñotambo during the un-retrofitted (field campaign in May 2015 [4]) and retrofitted (field campaign in December 2019) states.

		$V_p$ (m/s)	CoV (%)	$V_R$ (m/s)	CoV (%)	$E_{\text{dyn}}$ (MPa)	
Field Campaign May 2015	DA-1	380	7%	-	-	250	
	IA-1	-	6%	230	6%	290	
	IA-2	-	7%	220	7%	270	
	IB-1	-	36%	540	36%	1600	
Field Campaign December 2019	DA-1	350	15%	-	-	210	
	IA-1	-	-	280	33%	420	
	IB-1	-	-	540	19%	1600	
	NB	DB-1	520	3%	-	-	450
		DA-1	340	3%	-	-	200
	SB	DB-1	650	14%	-	-	720
		DA-3	500	11%	-	-	420

Abbreviations:  $V_p$ : P-wave velocity;  $V_R$ : R-wave velocity; A: Adobe masonry ( $n = 0.2$ ,  $r = 1900 \text{ kg/m}^3$  from [21]); B: Base course; rubble stone masonry with mud mortar ( $n = 0.2$ ,  $r = 1900 \text{ kg/m}^3$  from [22]); D: Direct sonic test; I: Indirect sonic test; N/A: Non-applicable; NB: North buttress; SB: South buttress.

Regarding adobe masonry, direct sonic tests on the north wall of the nave (DA-1) gave an  $E_{\text{dyn}}$  of  $210 \text{ MPa}$ , which is close to the  $250\text{--}290 \text{ MPa}$  values obtained during the May 2015 campaign. Indirect sonic tests on the exterior surface at the same location gave a much higher value ( $420 \text{ MPa}$ ). The difference is probably because the exterior adobe masonry layers were consolidated, and new adobe blocks replaced deteriorated ones, improving the condition of the exterior adobe masonry layers. Direct sonic tests of the adobe sections of the newly constructed south buttress (SB/DA-3) revealed the same  $E_{\text{dyn}}$  ( $420 \text{ MPa}$ ). Instead, a value of  $200 \text{ MPa}$  was registered from direct sonic tests on the adobe sections of the north buttress (NB/DA-1), which was only partially rebuilt.

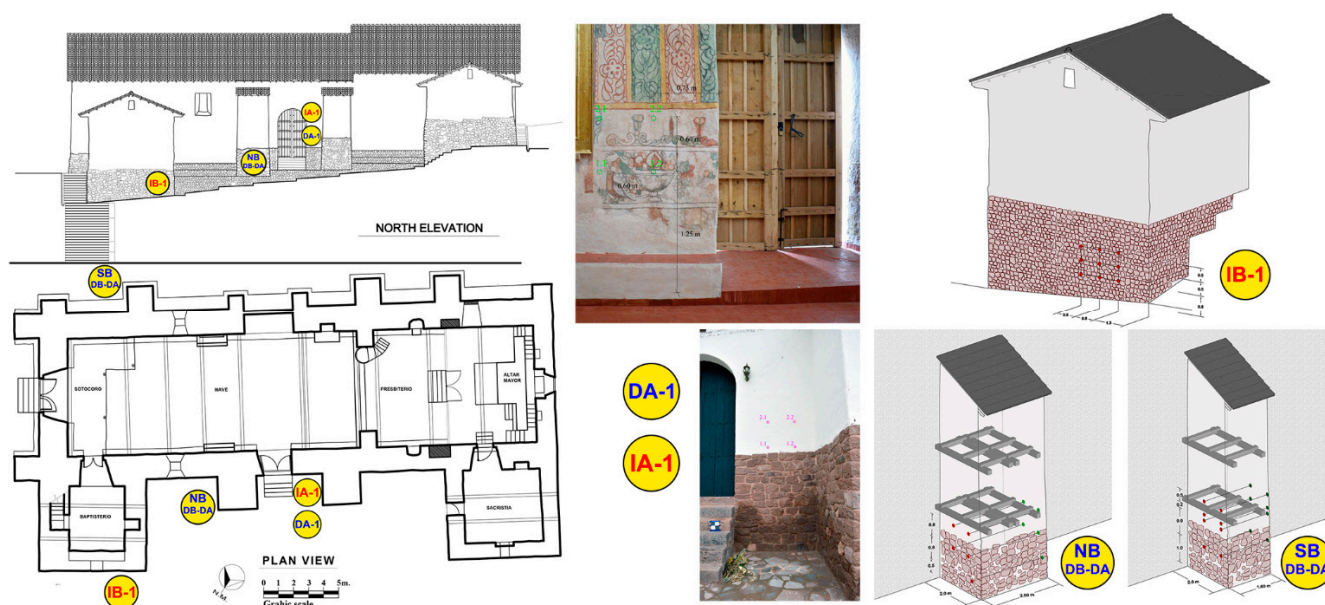


**Figure 12.** Retrofit state of the Church of Kuñotambo: location of direct and indirect sonic tests in adobe and rubble stone masonry during the December 2019 field campaign (after strengthening).

## 4. Finite Element Modeling

### 4.1. Modeling Approach

#### 4.1.1. General Description

In the analyses conducted, masonry was treated as a homogenous continuum material, since this approach is computationally efficient and gives valuable results when examining the global response of a building [23]. The use of a homogenized continuum tends to slightly overestimate capacity at large deformation levels because the softening functions used cannot accurately capture abrupt drops in load resistance, due to the formation of kinematic mechanisms involving the detachments of sections from the structure and posing high-level physical and geometrical nonlinearities [24]. A more accurate representation of such phenomena would require the discrete modeling of units and joints, which, however, is much more computationally demanding.

Based on a generated 3D CAD model, the commercial program DIANA with Midas FX+ Version 3.3.0 Customized Pre/Post-processor was utilized for generating and analyzing the FE model [25]. The numerical model was based on the 2015 model of the un-retrofitted structure [4], hereafter named MODEL\_0.

Two preliminary FE Models of the retrofitted Church of Kuñotambo were developed (Figure 13). In the first model, called MODEL\_1, full connectivity is assumed between parts. The FE mesh generated consists of 186,341 10-noded tetrahedron elements, with 3–4 elements per wall thickness, 18 two-noded truss elements for the tie beams and 1944 three-noded beam elements of various cross-sections, which represent the embedded timber strengthening elements [25]. The solid elements have an average edge size of 40 cm, while at the arched openings and niches, a more refined mesh with an element size of 20 cm was used. The second model, named MODEL\_2, accounts for the non-perfect continuity in masonry parts. This model has interfaces (highlighted in red in Figure 13b) representing (i) the connection of new buttresses with the nave wall, (ii) the connection of the east façade with the nave walls and (iii) two diagonal cracks at the south wall which could not be fully repaired due to the presence of wall paintings, which hindered complete sealing with grout injections [4]. The elastic stiffness properties of these interfaces are updating parameters, set for modal updating in the next sections. The number of elements is similar to MODEL\_1, with an additional 1435 plane triangular elements, with a mid-node, assigned to the interfaces.

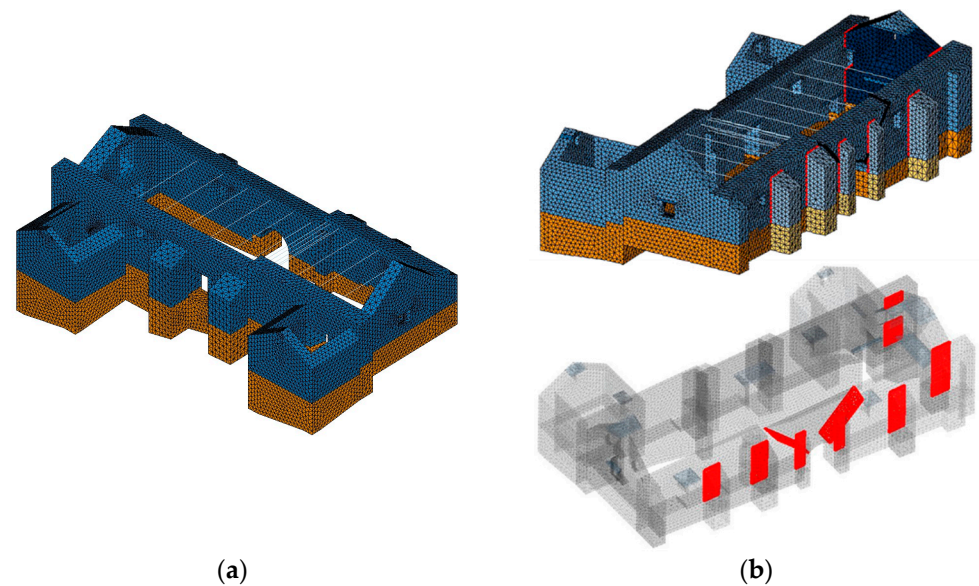


**Figure 13.** (a) Configuration of MODEL\_1; (b) Configuration of MODEL\_2. Note the definition of interfaces in red.

#### 4.1.2. Timber Elements

To feature only axial forces to the connection of the embedded timber frame, the ties were modelled as trusses. Embedded beam elements that take shear deformation into account were adopted for the other timber elements [25].

#### 4.1.3. Roof Loading

The new roof system is structurally independent and cannot provide any diaphragmatic stiffness due to the low stiffness at the connections. Hence, the roof was not included in the FE model, and only the resulting thrust was considered as an external load [4]. The roof's self-weight was applied as a distributed horizontal and vertical line load on the interior and exterior wall plates.

#### 4.1.4. Boundary Conditions and Interfaces

Fixed boundary conditions were defined for the base nodes of all models. The interface elements in MODEL\_2 are presented in Figure 13b. Interfaces in MODEL\_2 are assigned reduced normal and tangential stiffness values that were derived via model updating. As a starting point, it was considered that normal stiffness values for masonry are in the range of 10 to 100 N/mm<sup>3</sup> [23], with that of adobe possibly being one order of magnitude lower.

### 4.2. Nonlinear Material Properties

#### 4.2.1. Timber Elements

Nonlinear ideally plastic material models with different responses in tension and compression were used for modeling timber. The bending and shear capacities of the different cross-sections were also calculated and used for the post-processing of the numerical results in order to identify failure, based on permissible stresses. This modeling approach may be deemed oversimplifying given the anisotropic nature of timber and the influence posed by connections on the failure modes sustained. Nevertheless, it can provide a more detailed insight compared to the linear elastic modeling approach often adopted [26], since it can reasonably capture the overall behavior when the ductility of the connections between timber elements is greater than the capacity of the elements [27]. Timber-masonry interaction for embedded elements was also excluded from the analysis, as post-failure response is expected to be mostly governed by the early failure of masonry.

The average strength values adopted were computed through a probabilistic approach [28] considering that the timber used is Class B, as specified in the Peruvian Code [29]. In addition, in the intersections between timber members, half-lapped pinned connections were implemented. To account for the loss of capacity due to the reduction of the intersecting elements' cross-sectional area, the compressive and tensile strengths were halved (Table 2). Shear strength was not considered to decrease, as this type of failure is prevented at the areas of the connections by the presence of nails and pegs.

**Table 2.** Average and reduced values of strength in timber strengthening elements, with tie beams at free spans excluded.

Embedded Timber Elements		Tension		Compression		Shear
		Average yield stress Class B [MPa]	1/2 Average yield stress Class B [MPa]	Average yield stress Class B [MPa]	1/2 Average yield stress Class B [MPa]	Average yield stress Class B [MPa]
Section						
8' × 8'	20 × 20 cm <sup>2</sup>	41.0	20.5	33.5	16.7	5.87
6' × 6'	15 × 15 cm <sup>2</sup>					
4' × 4'	10 × 10 cm <sup>2</sup>					
3' × 6'	7.5 × 15 cm <sup>2</sup>		-		-	

The final strength values adopted for embedded timber strengthening elements were set by assigning a simple uniaxial yield stress criterion. The permissible tensile stress was thus set at 20.5 MPa, which is the estimated average tensile strength of the half section. The critical upper bound for compression was taken as the minimum value between the material compressive strength and the critical buckling load. Considering the tie beams in the free spans, the maximum permissible compressive stress was set at 10.2 MPa for tie beams of the nave, presbytery and altar and 24.1 MPa for those in the sacristy and baptistry.

#### 4.2.2. Adobe Masonry and Rubble Stone Masonry

A total strain rotating crack model is used to represent the physical nonlinear compressive and tensile behavior of masonry, with inelastic mechanisms developing from a diffused pattern of micro-cracks to localized macro-cracks [25]. The integral of the stress-displacement diagram, designated as fracture energy  $G_f$  for tension and  $G_c$  for compression [23], is used to quantify cracking and crushing, respectively. Compression includes a hardening and a softening phase, while tensile stresses decrease exponentially (Figure 14). Table 3 shows the applied mechanical characteristics, which have been based on the outcomes of the sonic tests and relevant data from the literature.

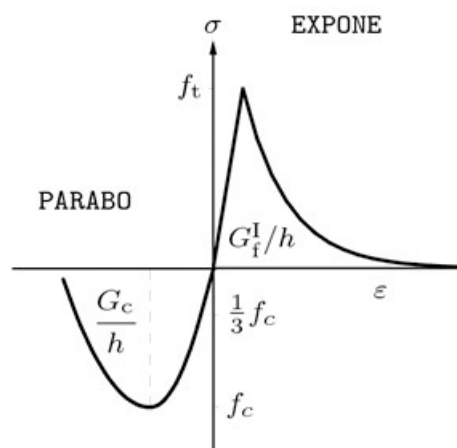


**Figure 14.** Stress/strain curve, showing the tensile and compressive behavior of masonry [25].

**Table 3.** Mechanical properties of adobe masonry, rubble stone masonry and timber elements.

Mechanical Properties	Unit	Adobe Masonry	New Adobe Masonry	Rubble Stone Masonry	New Rubble Stone Masonry	Timber	
						Class B	Lintels <sup>1</sup>
Modulus of elasticity	E (MPa)	272 <sup>2</sup>	272 <sup>2</sup>	530 <sup>2</sup>	530 <sup>2</sup>	9806 <sup>7</sup>	10,680
Specific weight	$\gamma$ (KN/m <sup>3</sup> )	19 <sup>3</sup>	19 <sup>3</sup>	19 <sup>4</sup>	19 <sup>4</sup>	5.6 <sup>7</sup>	4.8
Poisson's ratio	$\nu$	0.2	0.2	0.2	0.2	0.2	0.2
Compressive strength	$f_c$ (MPa)	0.45	1.0	0.6	1.0	10.8 <sup>5,7</sup>	38.1 <sup>5</sup> /6.3 <sup>6</sup>
Tensile strength	$f_t$ (MPa)	0.05	0.06	0.01	0.06	10.3 <sup>5,7</sup>	14.7
Fracture energy (tension)	$G_f$ (N/mm)	0.01	0.01	0.01	0.01	-	-
Fracture energy (compression)	$G_c$ (N/mm)	1	2	1.5	3	-	-

<sup>1</sup> Oregon pine timber species with a high Young's modulus was chosen, in order to avoid excessive concentration of stresses and deformations [30]; <sup>2</sup> Sonic tests; <sup>3</sup> Sanchez et al. 2022 [21]; <sup>4</sup> NTC 2018 [22]; <sup>5</sup> Parallel to grain; <sup>6</sup> Perpendicular to grain; <sup>7</sup> Norm E.010 [29].

## 5. Modal Updating

### 5.1. Introduction

FE model updating emerged as a key topic in the design, construction and maintenance of structures [18]. A discussion on direct and iterative methods for FE model updating can be found in [31–34]. In FE model updating based on AVT, an optimization problem is set up to minimize differences between the experimentally derived and the numerically computed modal data. Reference is made to [31,32] regarding the use of gradient-based methods, response surface methods and nature-inspired algorithms for solving the optimization problem.

In the current study, the natural frequencies and the mode shapes were taken from AVTs, while the FE model updating technique was performed using MATLAB codes interfaced with DIANA FEA, using the Douglas–Reid method [35]. The latter approximates the natural frequencies of the model with a specified function of the unknown structural parameters. In the following sections, the process to obtain the calibrated models is discussed using both MODEL\_1 (no interfaces) and MODEL\_2 (with interfaces).

### 5.2. Modal Analysis

A modal analysis was performed for models MODEL\_1 and MODEL\_2, with the material properties of Table 3. For MODEL\_2, the initial values for the interfaces are presented in Table 4. The obtained mode shapes of the first nine modes are presented in Figures 15 and 16. The structure in its un-retrofitted state had severe damage, including vertical fragmentation cracks at wall intersections, which the FE model with full connectivity at corner junctions does not depict [4]. However, a comparison of the retrofitted model to the model with no strengthening and no damage reveals a clear shift in modal participation masses in the y–y direction (N-S), towards higher modes. This is mostly attributed to the installation of buttresses in that direction as well as the simultaneous stimulation of the nave's lateral walls, by means of the timber strengthening elements.

The numerically computed mode shapes are compared against those obtained from the dynamic identification tests (Figure 11). The first transversal mode involves mainly out-of-plane movement of the lateral nave walls. Here, the strengthened structure is found to be stiffer and is excited at higher resonant frequencies. Due to the presence of timber strengthening elements, both lateral nave walls are excited in a symmetric in-phase pattern. The connectivity in the corners, the anchoring of the tie beams, the bond beam and timber keys, both orthogonal and horizontal, have resulted in higher stiffness and approximating a favorable box behavior [36]. Instead of the previous complex out-of-plane bending modes of the nave and presbytery, the retrofitted structure presents in-plane bending modes of

single curvature, in this case, Mode 2 (3.68 Hz) and Mode 3 (4.55 Hz). Hence, Mode 2 from the AVT is closely correlated with Mode 2 (4.50 Hz) from MODEL\_1 and Mode 1 (3.70 Hz) from MODEL\_2.

**Table 4.** Preliminary material properties in the elastic range for MODEL\_1 and MODEL\_2.

Materials	$E_{\text{mod}}$ Base Course (GPa)	$E_{\text{mod}}$ Adobe Walls (GPa)	Normal Stiffness Interface East Façade (N/mm <sup>3</sup> )	Normal Stiffness Interface Buttresses (N/mm <sup>3</sup> )	Normal Stiffness Interface Crack at Arch Span (N/mm <sup>3</sup> )
MODEL_1	1.56	0.27	-	-	-
MODEL_2	0.35	0.475	0.018 *	1.8 *	0.18 *

\* Note that the tangential stiffness of the interface is taken equal to 40% of the normal one, considering a Poisson ratio of 0.2.

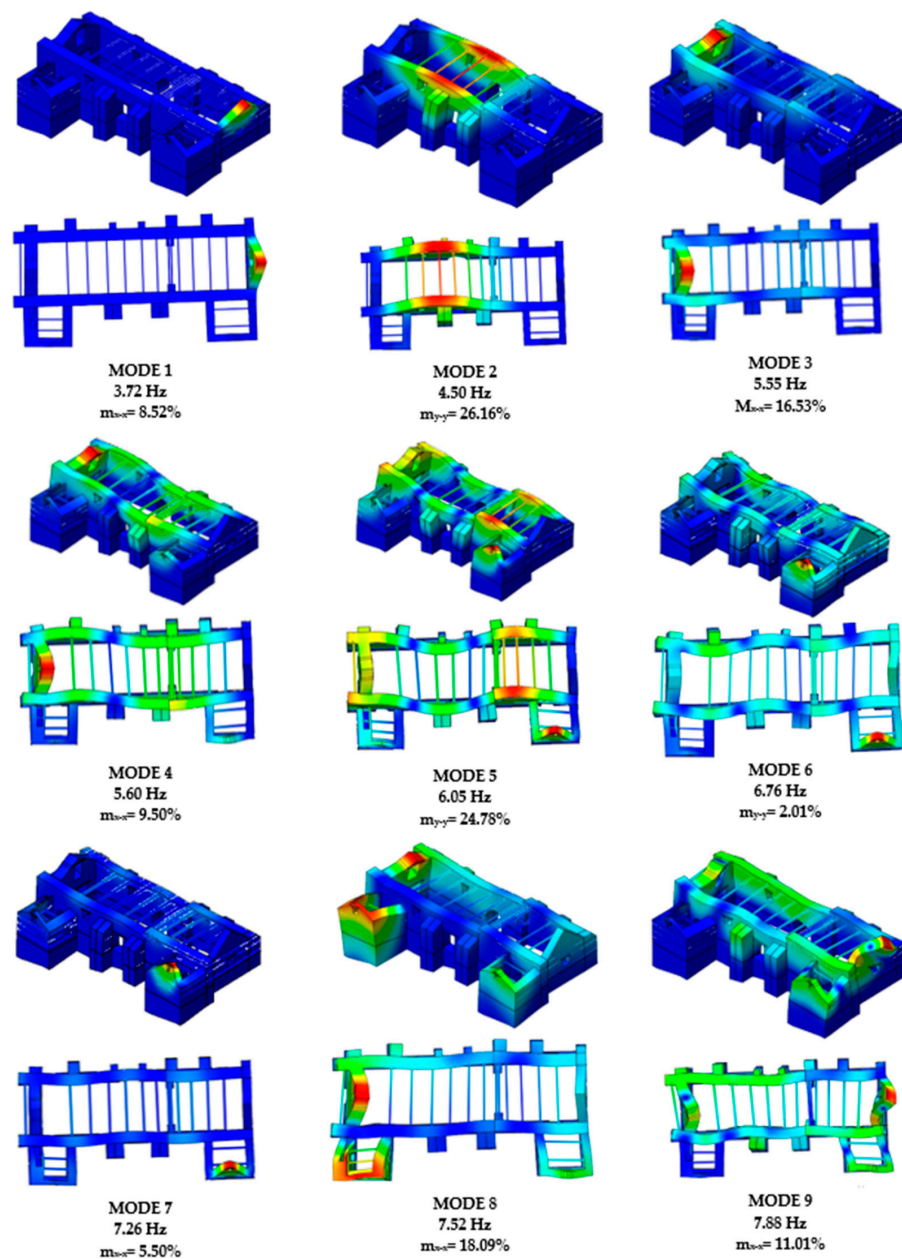


**Figure 15.** Selected modes from the modal analysis, for the retrofitted model MODEL\_1.



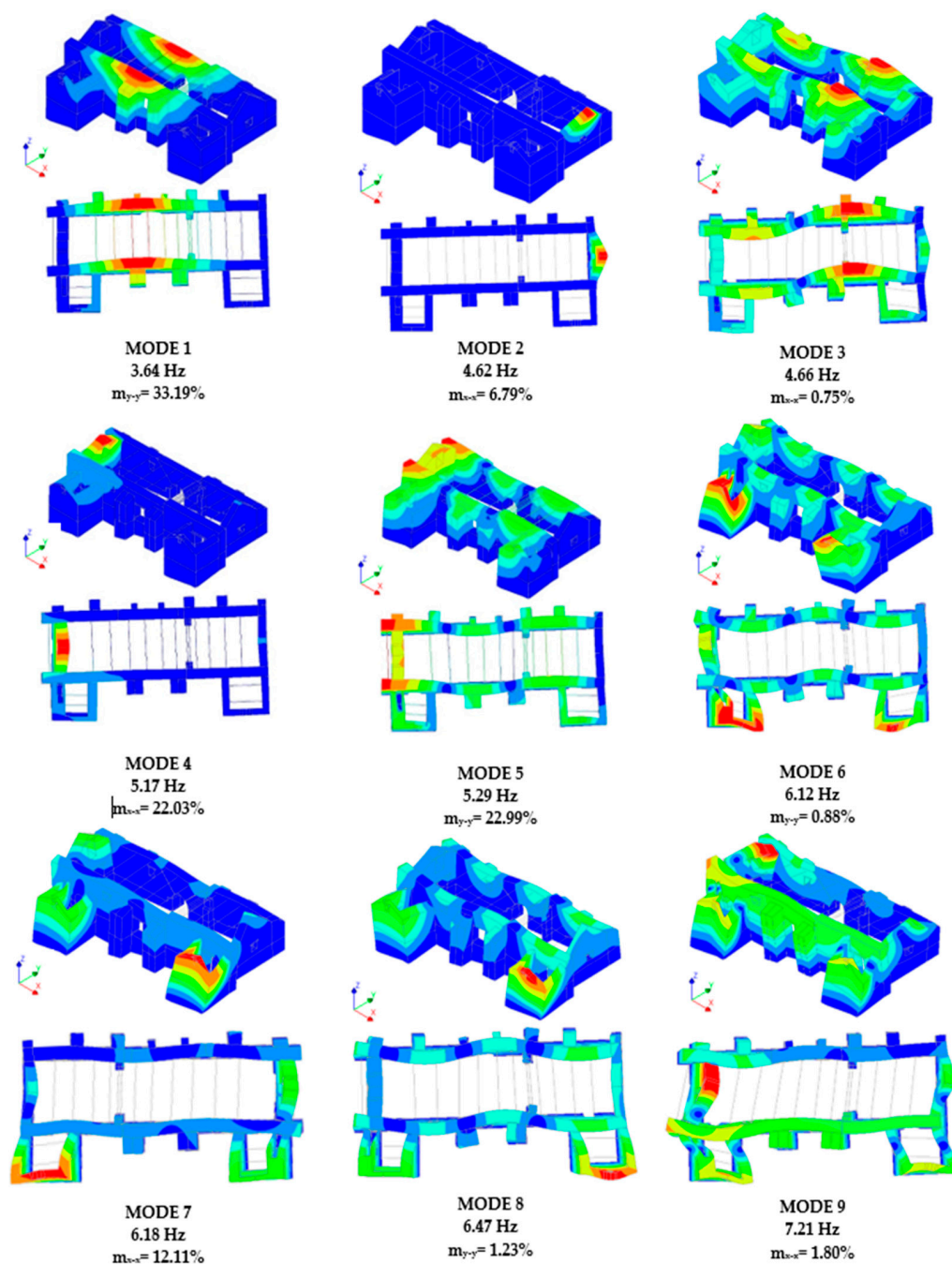


**Figure 16.** Selected modes from the modal analysis, for the retrofitted model MODEL\_2.

The additional stiffness from the reconstructed *quincha* arch, the asymmetrically constructed new buttresses on the south façade, the extended free height of the nave's lateral walls and the elevated ground floor leading to the altar appear to divide the out-of-plane modes of the nave. The presbytery's walls appear to be stiffer than the ones of the nave, being excited at a higher frequency of 4.55 Hz (Mode 3 in Figure 11). Hence, Mode 3 (5.55 Hz) of MODEL\_1 and Mode 2 (4.62 Hz) of MODEL\_2 can be considered a potential match.

Experimentally derived Mode 5 (5.31 Hz) corresponds to an out-of-plane bending mode of the nave and presbytery walls, in a second order of curvature. The actual mode is very well represented by the FE models, with a difference in frequency of 13% in Mode 5 of MODEL\_1 (6.05 Hz) and 1% in Mode 5 of MODEL\_2 (5.29 Hz). Regarding the principal out-of-plane mode of the east façade, Mode 4 (5.26 Hz) of the AVT is configured under a

single curvature. The current mode is captured efficiently by both models, with a difference in frequencies of 5% in Mode 3 of MODEL\_1 (5.60 Hz) and 2% in Mode 4 of MODEL\_2 (5.17 Hz). With a higher frequency of 6.31 Hz, the Mode 6 of the AVT involves out-of-plane deflection of the east and west gable ends of the nave and altar, respectively. Such a response is not captured by MODEL\_1, nor by MODEL\_2. This mode might be triggered by the interaction with the roof, whereas in the FE models the roof is ignored. Mode 9 (11.43 Hz) involves only out-of-plane bending of the west gable end, at a much higher frequency compared to the results of Mode 9 of MODEL\_1 and MODEL\_2, with frequencies of 7.88 and 7.21 Hz, respectively. The difference in corresponding frequencies is 85%, which clearly indicates that the west façade is stiffer. Such an increase can be influenced by the additional stiffness from the roof and the transversal timber connections with the timber altar piece, covering the entire interior elevation.

Thus, considering the above, the following pairs of modes are considered for the modal updating process:

- Mode 2 equal to 3.68 Hz of the AVT, Mode 2 equal to 4.50 Hz of MODEL\_1 and Mode 1 equal to 3.64 Hz of MODEL\_2;
- Mode 4 equal to 5.26 Hz of the AVT, Mode 3 equal to 5.55 Hz of MODEL\_1 and Mode 4 equal to 5.17 Hz of MODEL\_2;
- Mode 5 equal to 5.31 Hz of the AVT, Mode 5 equal to 6.05 Hz of MODEL\_1 and Mode 5 equal to 5.29 Hz of MODEL\_2.

### 5.3. Modal Updating Procedure

Modal updating involved the calibration of material elastic properties, with the objective of obtaining the modal frequencies of the three selected modes. Upper and lower limits were established for the properties that were examined in the framework of the modal updating procedure.

First, for the calibration variables of MODEL\_1, the Young's modulus of the adobe walls and the stone base course were considered. Next, the initial values of Young's modulus for the adobe walls and the base course were set according to the ones obtained from the in situ sonic tests. The upper and lower limits for the calibration variables of MODEL\_1 are presented in Table 5. For MODEL\_2, four updating variables were considered (Young's moduli of the adobe, base course and façade masonries and normal stiffness of interfaces), with upper and lower limits shown in Table 6. Here, it is noted that the higher initial and updated value for the Young's modulus of the façade was considered, given the higher correlation with the experimental AVTs results. Such a difference can be justified under a more elaborate construction process and/or less damage present.

**Table 5.** Upper and lower limit values for calibration for MODEL\_1, with the corresponding frequencies, for the selected modes.

Variable	Modulus of Elasticity (GPa)	Lower Limit (GPa)	Upper Limit (GPa)	Updated Values (GPa)
Base Course	1.56	0.53	3	0.53
Adobe Walls	0.27	0.1	0.54	0.272
MODE 2 (Hz)	-	3.06	4.84	3.68
MODE 4 (Hz)	-	3.69	5.67	5.15
MODE 5 (Hz)	-	4.07	6.42	5.23

The updated modes from the calibrated models are included in Figure 17. The first mode has the same frequency as that from the AVT, while the error is lower than 3% for the other two modes.

**Table 6.** Upper and lower limit values for calibration for MODEL\_2, with the corresponding frequencies, for the selected modes.

Variable	Modulus of Elasticity (GPa) [1]/Normal Interface Stiffness (N/mm <sup>3</sup> ) [2]	Lower Limit (GPa)	Upper Limit (GPa)	Updated Values (GPa)/(N/mm <sup>3</sup> )
Base Course	0.35 [1]	0.32	0.70	0.41
Adobe Walls	0.475 [1]	0.25	0.45	0.39
Facade	0.70 [1]	0.60	1.10	0.60
Façade Interface	0.018 [2] *	0.0018	0.126	0.040
MODE 1 (Hz)	-	3.43	4.18	3.69
MODE 4 (Hz)	-	5.12	5.90	5.17
MODE 5 (Hz)	-	5.34	6.02	5.31

\* Note that the tangential stiffness of the interface is taken equal to 40% of the normal one, considering a Poisson ratio of 0.2.

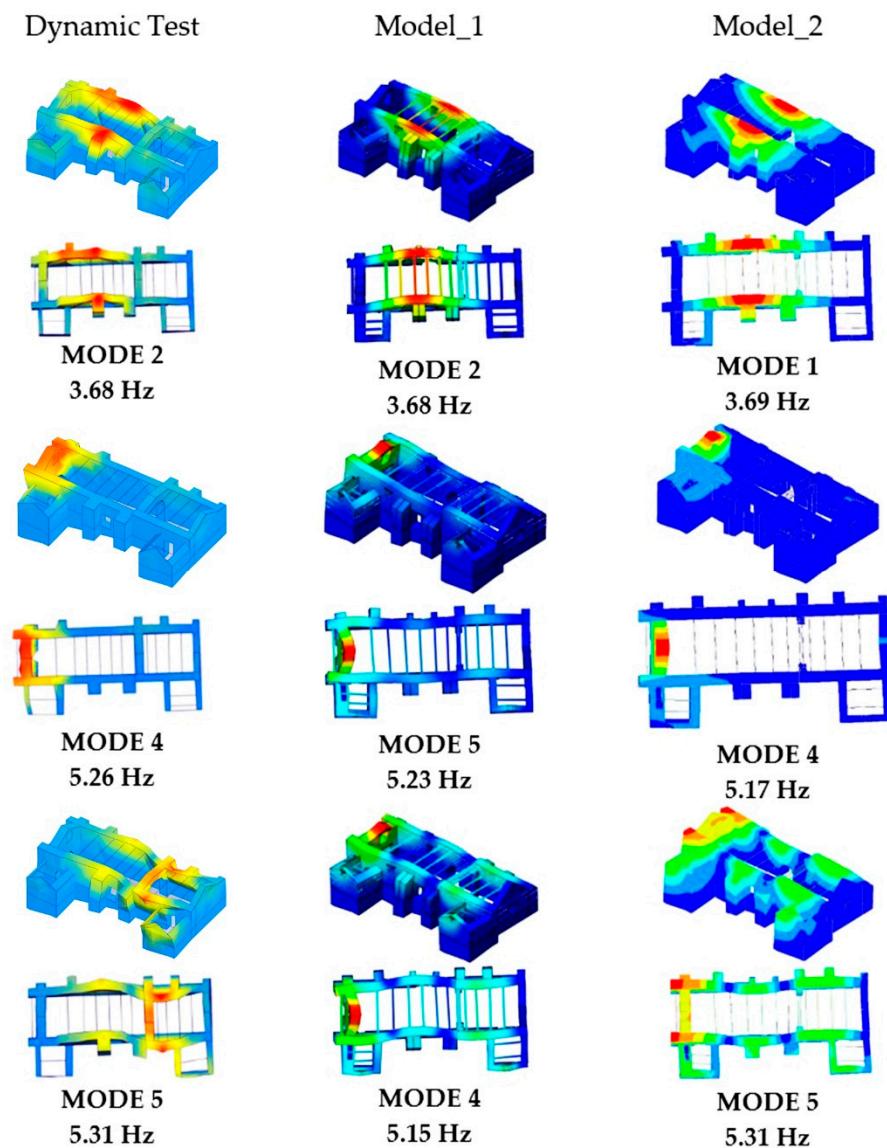


**Figure 17.** Mode shapes of the selected modes in MODEL\_1 and MODEL\_2, as obtained from the updated numerical models, in comparison with the modal shapes of the dynamic tests, for the retrofitted church.

The Modal Assurance Criteria (MAC), given by Equation (1), was used to calculate the correlation between the mode shape vectors obtained from the updated models and the AVT [37]. Here,  $\varphi_u$  and  $\varphi_d$  are the mode shape vectors for the two different modal conditions and  $n$  is the number of degrees of freedom, hence, the positions of the accelerometers and the corresponding nodes of the numerical models. Uncorrelated (orthogonal) and perfect matching vectors between the two mode shapes are implied by MAC values equal to 0 and 1, respectively. Results are presented in Tables 7 and 8.

$$MAC_{u,d} = \frac{\left| \sum_{i=1}^n \varphi_i^u \varphi_i^d \right|^2}{\sum_{i=1}^n (\varphi_i^u)^2 \sum_{i=1}^n (\varphi_i^d)^2} \quad (1)$$

**Table 7.** MAC values for MODEL\_1 and AVT.

Dynamic Test FE Model	Mode 2 (3.68 Hz)	Mode 4 (5.26 Hz)	Mode 5 (5.31 Hz)
Mode 1 (3.68 Hz)	0.63	0.01	0.00
Mode 5 (5.23 Hz)	0.00	0.33	0.26
Mode 4 (5.15 Hz)	0.01	0.46	0.60

**Table 8.** MAC values for MODEL\_2 and AVT.

Dynamic Test FE Model	Mode 2 (3.68 Hz)	Mode 4 (5.26 Hz)	Mode 5 (5.31 Hz)
Mode 1 (3.65 Hz)	0.90	0.04	0.08
Mode 4 (5.15 Hz)	0.00	0.61	0.01
Mode 5 (5.30 Hz)	0.16	0.02	0.81

MODEL\_2 presents the highest MAC values for all three selected modes. For Mode 1, the MAC value of 0.90 denotes an almost perfect correlation. For Modes 4 and 5, the MAC values are still high (0.61–0.80) when only the nave, presbytery and altar walls are considered. Instead, the correlation of the updated MODEL\_1 with the documented behavior is considered rather weak, with MAC values ranging between 0.33–0.63. Hence, accounting discontinuities, cracks and non-perfect connections appear to interpret more accurately the real behavior of the retrofitted church. Consequently, MODEL\_2 is chosen as the representative model for the following nonlinear FE analyses.

## 6. Nonlinear Static Analysis

In the process of structural assessment for masonry structures, with 3D FE macro-models, certain idealizations can be adopted, e.g., material nonlinearities are accounted for, with masonry assumed as an isotropic material; geometric nonlinearities and effects of different loading cases are often disregarded; and seismic, equivalent lateral loads are monotonically increasing [23]. In particular, in masonry structures with relatively uniform regularity in plan and elevation, and considering a uniform mass distribution, seismic actions are simplified under a lateral loading, applied conventionally using a mass-proportional approach, and following the primary directions of the structure. Nonlinear static analyses progress until a certain level of damage is captured, at a point of the post peak, indicative of a collapse mode.

Instead, nonlinear dynamic analyses (NDA) account for complete 3D earthquake acceleration time histories and are considered more accurate, yet, under high computational demands. As outlined in [4], for simple masonry buildings, the superposition of tensile damage patterns from nonlinear pushover analyses and NDA are under good agreement, with the latter configured with a more diffused pattern. As shown in [38], in highly complex

and irregular masonry buildings, a multidirectional pushover analysis (MDPA), under different earthquake loading directions, can provide a more inclusive representation of collapse failure mechanisms.

Nonlinear, mass-proportional pushover analyses of the retrofitted structure were performed in all four principal directions (+Y, −Y, +X, −X). For each direction, the pushover curves of three different FE models are presented. Results refer to (i) the un-retrofitted FE model (MODEL\_0) as the reference for assessment, (ii) the updated MODEL\_2 and (iii) MODEL\_3, which has the same material properties with updated MODEL\_2, except for the interfaces that have been made rigid to represent fully restored connections. It is noted that for the pushover curves in each direction and analysis step, the sum of the corresponding base shear and the lateral displacement from a node presenting the maximum deflection were chosen. In addition, given the lower correlation with the experimental modal frequencies for the updated Model\_1, and the corresponding updated lower stiffness of the adobe walls, FE analysis results are not presented and are considered of low accuracy.

As shown in Figure 18a, the capacity of the un-retrofitted church in the +YY direction, is less than the region's 0.25 g design peak ground acceleration [14]. The maximum estimated capacity of MODEL\_2 is equal to 0.33g, which surpasses the capacity demand for the region. From the plots of the maximum principal tensile strains, presented in Figure 19a, it is evident that the strengthened structure presents a more global failure mode, which consists of out-of-plane bending of both lateral walls, together with diagonal and vertical shear cracks in the side walls of the baptistery, the sacristy and the east façade. The more homogenous structural response is mainly the result of the bracing timber elements. These prevented the early separation and out-of-plane overturning of the south lateral wall that occurred in MODEL\_0.

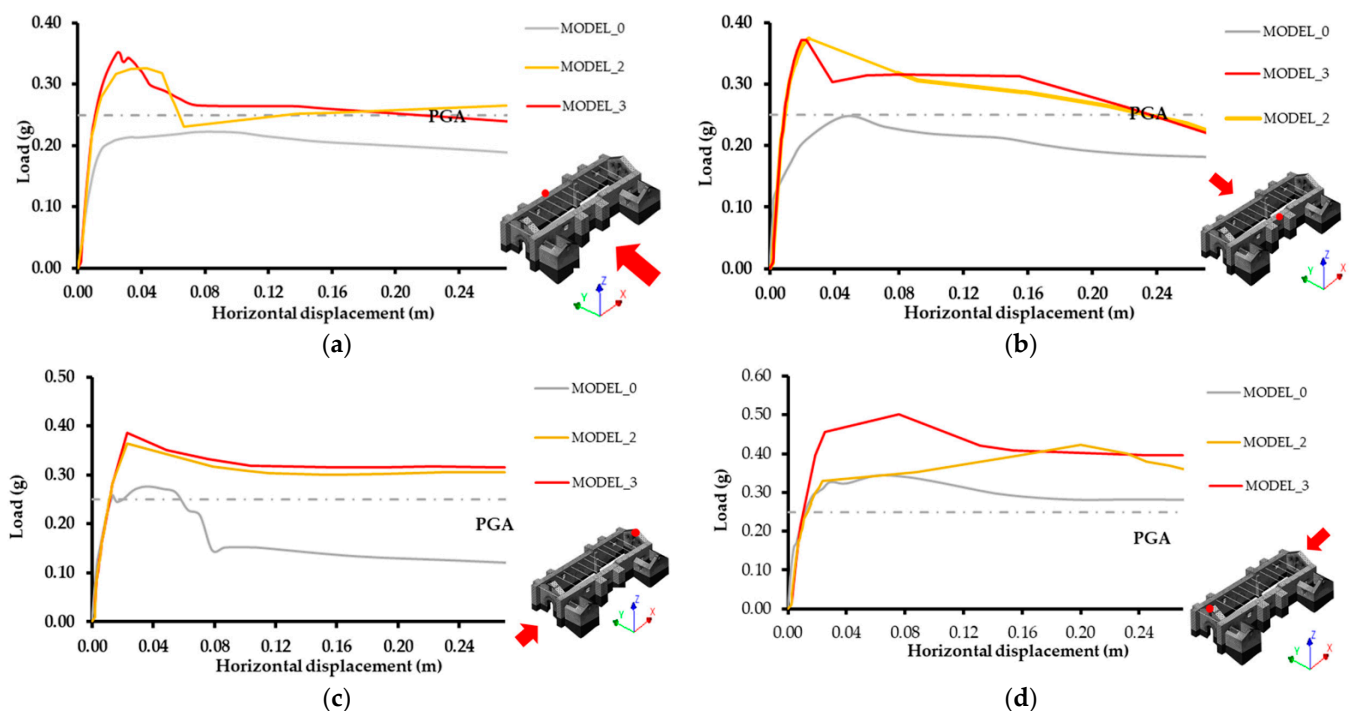


**Figure 18.** Pushover curves of Models 0, 2 and 3 in (a) +YY, (b) −YY, (c) +XX and (d) −XX directions. Note that the displacements in the pushover curves correspond to the displacements of the control nodal points, indicated here with red dots.

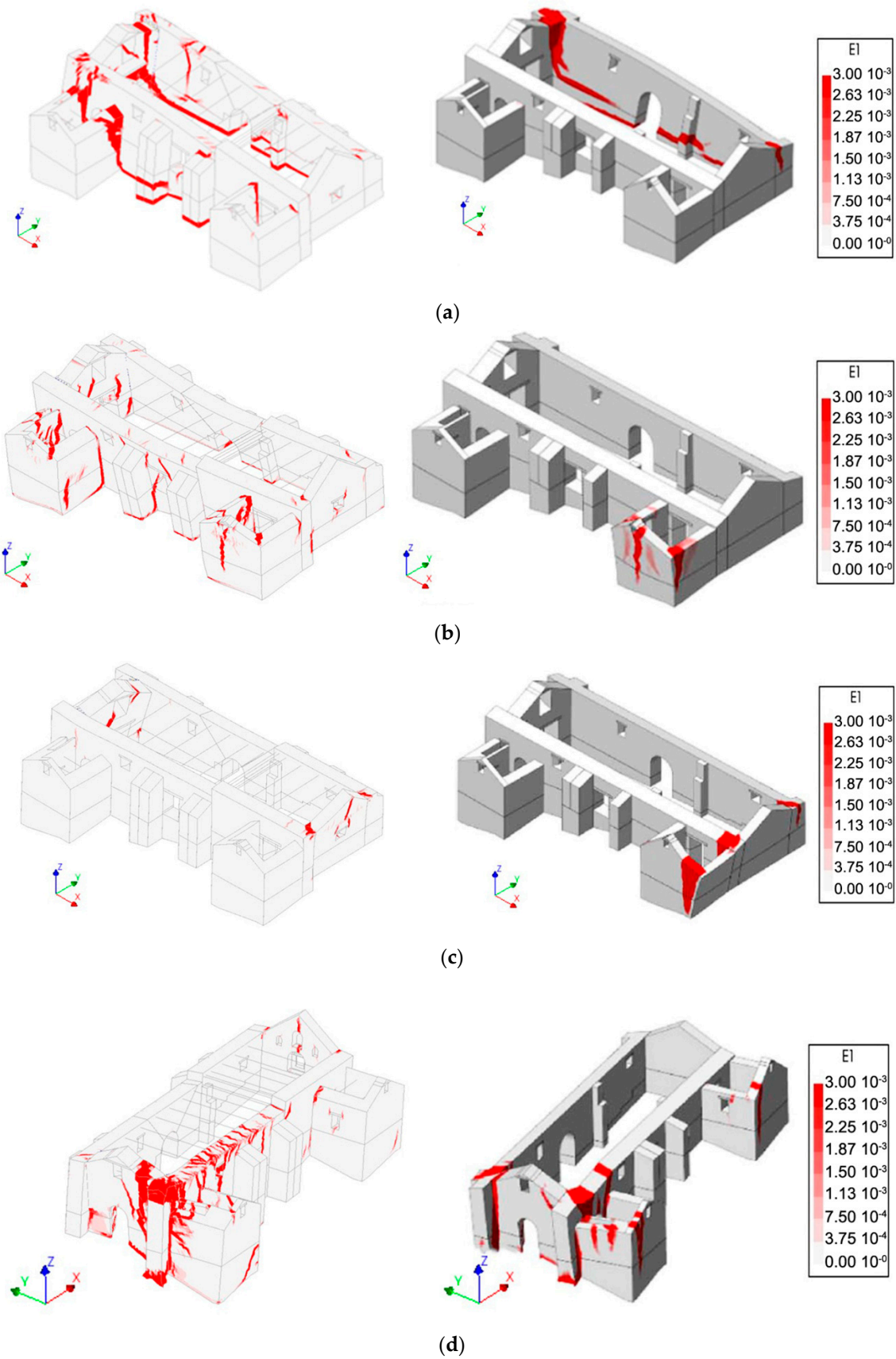


**Figure 19.** Distribution of maximum principal tensile strains at maximum capacity for MODEL\_2 (left) and MODEL\_0 (right) in (a) +YY, (b) -YY, (c) +XX and (d) -XX directions.

The pushover curves in the negative  $-YY$  direction (Figure 18b) indicate that the un-strengthened MODEL\_0 barely reached the capacity of 0.25 g, while both strengthened models MODEL\_2 and MODEL\_3 attained a capacity of approximately 0.37 g. This clearly evidences the effectiveness of the strengthening. MODEL\_3 and MODEL\_2 exhibit similar behavior, despite the actual difference in the values of elastic stiffness at interfaces. In fact,  $-YY$  is the weak direction for out-of-plane behavior in the south lateral wall of the nave, presbytery and altar. Thus, considering the lower counteracting resistance of the south buttresses, the south wall in both models fails mainly under the same diagonal in-plane flexural cracks and a tensile rotation failure zone at the base, and hence the stiffness of the assigned interfaces presents a lower influence in the resultant lateral capacity.

The computed distribution of maximum principal tensile strains plots (Figure 19b) indicates that in MODEL\_0, failure in the  $-YY$  direction is characterized by out-of-plane rotation and vertical bending fragmentation of the gable wall of the sacristy. The presence of the timber strengthening elements in MODEL\_2 results in a global failure mode, which involves out-of-plane bending of the lateral walls, together with the development of in-plane shear cracks in the side walls of the baptistery and sacristy, and the east façade. It is noted that the vertical cracking shown in the side base course walls of the sacristy is identical to the documented damage in situ (2.5 in Figure 7).

In the  $+XX$  direction (Figure 18c), the capacity of MODEL\_0 marginally exceeds the limit of 0.25 g, but a sharp post-peak reduction of lateral resistance occurs. The capacities of MODEL\_2 and MODEL\_3 were both approximately equal to 0.37 g. Referring to Figure 19c, failure in MODEL\_0 consists of out-of-plane rotation of the entire west façade after it disconnects from the nave walls. Instead, the corresponding failure mode in MODEL\_2 also involves the east façade, with cracking at the corners to a lesser extent and vertical bending fragmentation at both gable ends.

Lastly, in the  $-XX$  direction (Figure 18d), the capacity at peak for MODEL\_0 was equal to 0.32 g, with a relatively small slope in the post peak, reaching by minimum 0.27 g. Peak capacity in MODEL\_2 increased to 0.42 g, with slight hardening up to 20 cm of lateral displacement, attributed to the axial elongation of the bond beams in the lateral walls. Considering that the façade was strengthened only with orthogonal corner keys and no bond beam, it can be argued that significant improvement was achieved. MODEL\_3 reached a peak capacity of 0.50 g, which decreased smoothly to around 0.40 g at the ultimate stage.

According to the contours of Figure 19d, the failure of MODEL\_0 involves out-of-plane rotation of the east façade and vertical shear cracking of the nave's lateral walls. This is consistent with that observed in the damage assessment of [4]. After strengthening, the damage is mostly concentrated in the north end of the east façade, due to the asymmetric distribution of stiffness within the plan of the building and the presence of an opening and lintel on the north side. In addition, parallel vertical cracks occur at the top of the north lateral nave wall, indicating the axial elongation of the bond beam that was installed. The damage at the peak capacity, in this case, is rather extensive but it is also more widely distributed.

Comparing the axial, bending and shear loads computed for the timber strengthening elements, it is noted that values in  $+Y$  and  $-Y$  directions are generally higher than in the  $+X$  and  $-X$  directions, with the exception of local maxima. In the  $Y-Y$  direction, the maximum axial force is 400 kN, occurring in the tie beam of the front façade. In terms of the shear, the maximum force was 64 kN and it also occurred in the bond beams in the corner of the front façade. In the  $X-X$  direction, the maximum axial force reached 400 kN in the first two tie beams near the front façade. The maximum shear is 133 kN in the bond beams in the front façade. The maximum moment in this direction is 16 kN.m in the bond beams of the baptistery. For both principal directions analyzed, no failure of timber members was detected with respect to the estimated capacities reported in Section 4.2.1. Shear damage was only predicted for a corner key of the southeast corner junction when this reached

90 kN after 12 cm of displacement in the  $-XX$  direction. Yet, this is considered to be a local failure.

## 7. Performance Based Seismic Assessment

Expressing seismic demand in terms of displacements linked to different limit states is hereby discussed following the work of Illampas et al. 2020 [39]. The process of calculating the displacement demand for a given spectra requires the transformation of the multi-degree-of-freedom (MDOF) to an equivalent single-degree-of-freedom (SDOF) system. An important aspect, before the transformation to a SDOF system, lies in the definition of the ultimate displacement in each direction. Calculating the ultimate displacement associated with out-of-plane failures in masonry buildings is not straightforward, with a comparative process followed, accounting for the recommendations from three different building codes, i.e., the ASCE41-13 [40], the NTC 2018 [22] and the KADET (2021) [41].

In ASCE41-13 [40], for reinforced masonry buildings, out-of-plane drift ratios  $\leq 5\%$  are prescribed for the Near Collapse (NC) state, while for the life safety (LS) condition, drift ratios  $\leq 3\%$  are defined. In KADET 2021 [41], the out-of-plane drift at failure from overturning is taken equal to  $0.003 H_0/t$ , where  $H_0$  and  $t$  are the height and thickness of the wall, respectively [42]. In NTC 2018 [22], the NC condition is defined by a 15% force drop after the peak in the pushover curve. The basic geometric inputs used, involve a wall height of  $H_0 = 9$  m, taken at the middle of the wall with the highest out-of-plane displacement, and a masonry thickness of  $t = 1.7$  m, which is constant for the walls of the nave, presbytery and altar. Thus, the ultimate displacement according to KADET 2021 and ASCE41-13 is 15.9 cm and 27.0 cm, respectively (Figure 20). By comparing the minimum and maximum principal strains at the stage when the ultimate displacements calculated by the different codes are reached (Figures 21–24), the ASCE41-13 method was chosen as more representative of the damage expected in a Near Collapse condition.

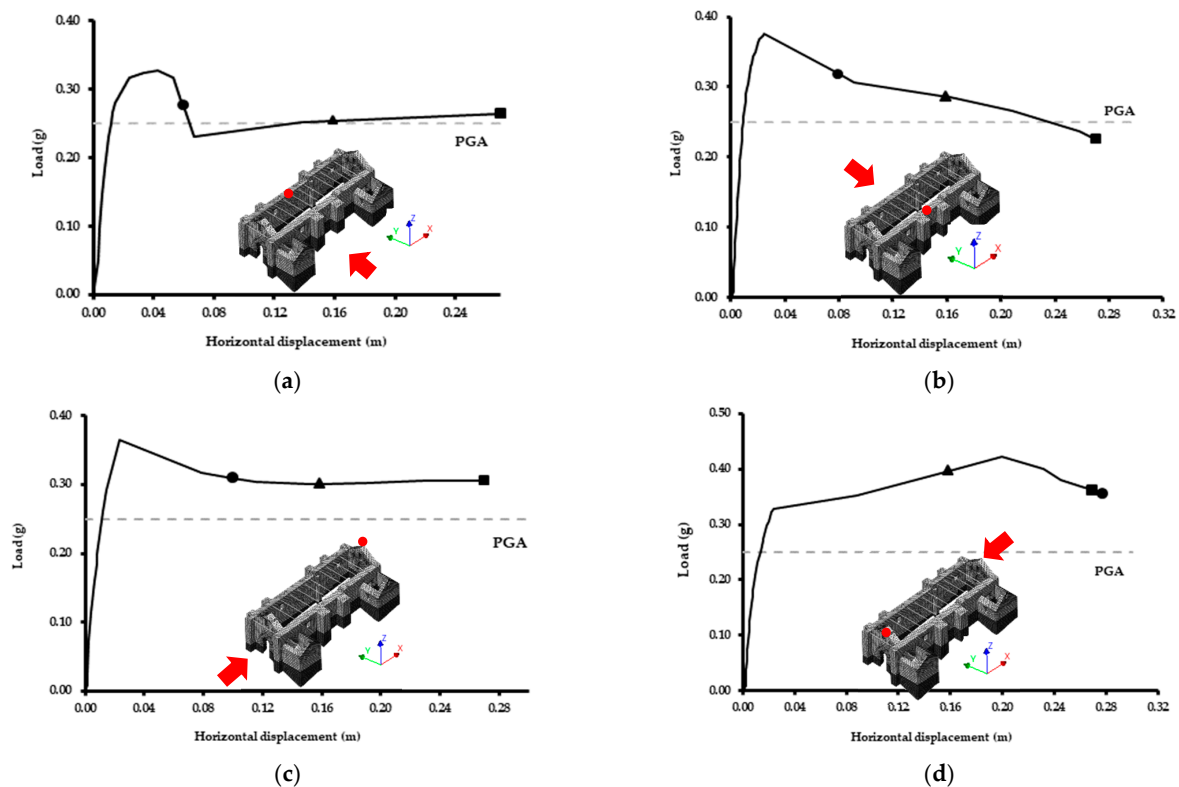


**Figure 20.** Pushover curves in different directions: (a) +YY, (b) -YY, (c) +XX and (d) -XX. Here, the representative points for the ASCE41-13 (■), NTC 2018 (●) and KADET 2021 (▲) are presented.



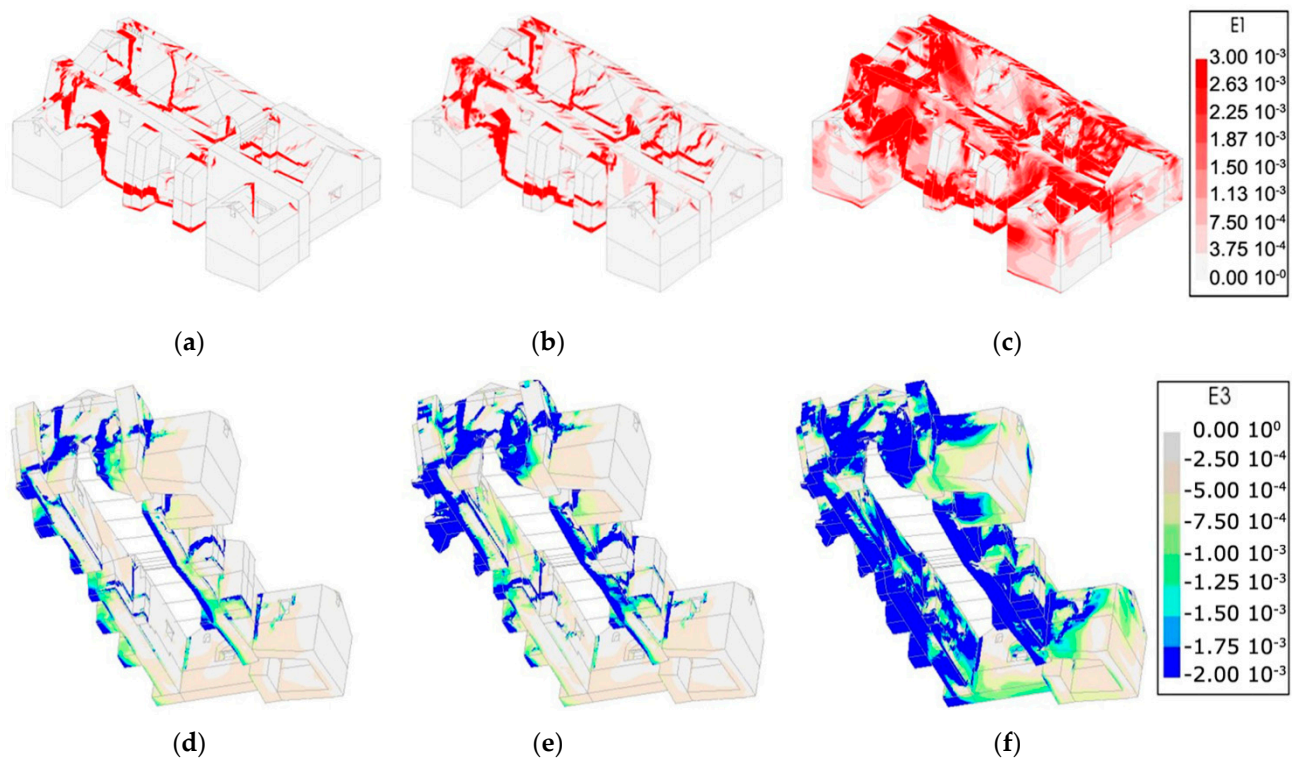


**Figure 21.** Distribution maximum principal strain in +YY direction at the ultimate stage of (a) NTC 2018, (b) KADET 2021 and (c) ASCE41-13. Distribution minimum principal strain in +YY direction at the ultimate stage of (d) NTC 2018, (e) KADET 2021 and (f) ASCE41-13.

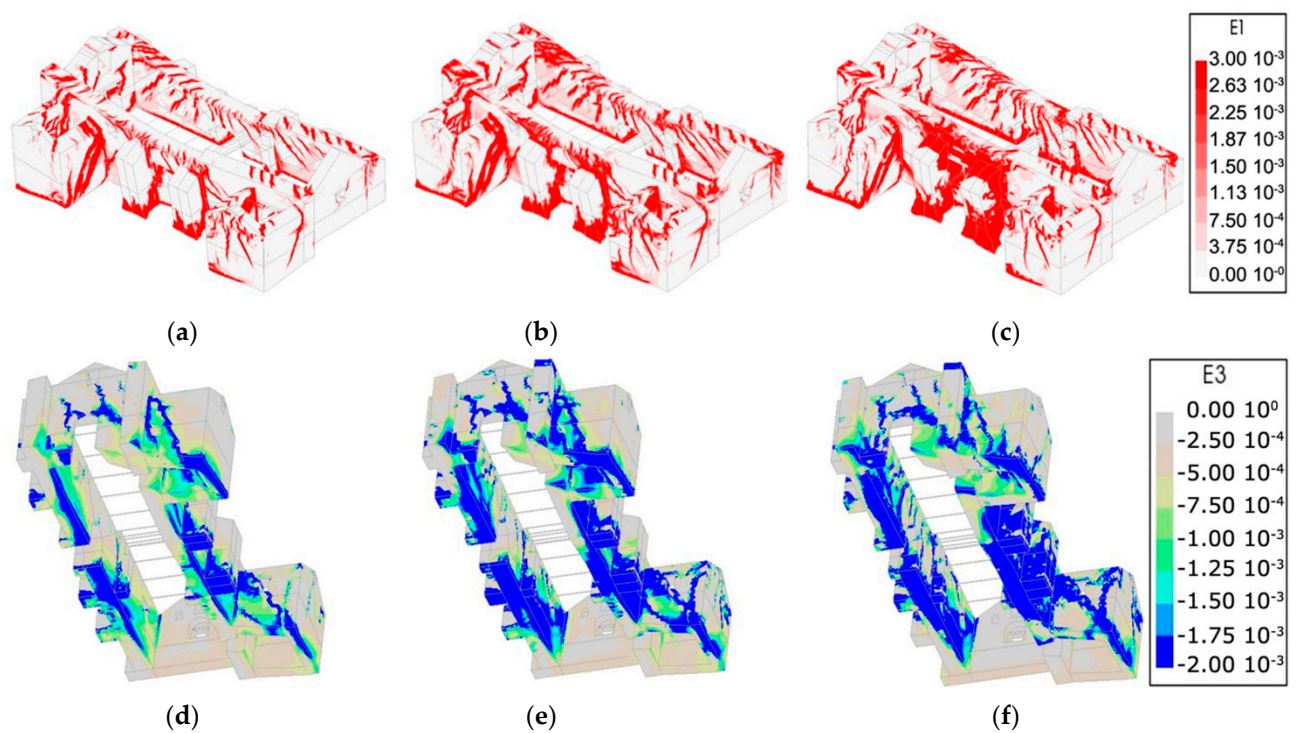


**Figure 22.** Distribution maximum principal strain in  $-YY$  direction at the ultimate stage of (a) NTC 2018, (b) KADET 2021 and (c) ASCE41-13. Distribution minimum principal strain in  $-YY$  direction at the ultimate stage of (d) NTC 2018, (e) KADET 2021 and (f) ASCE41-13.

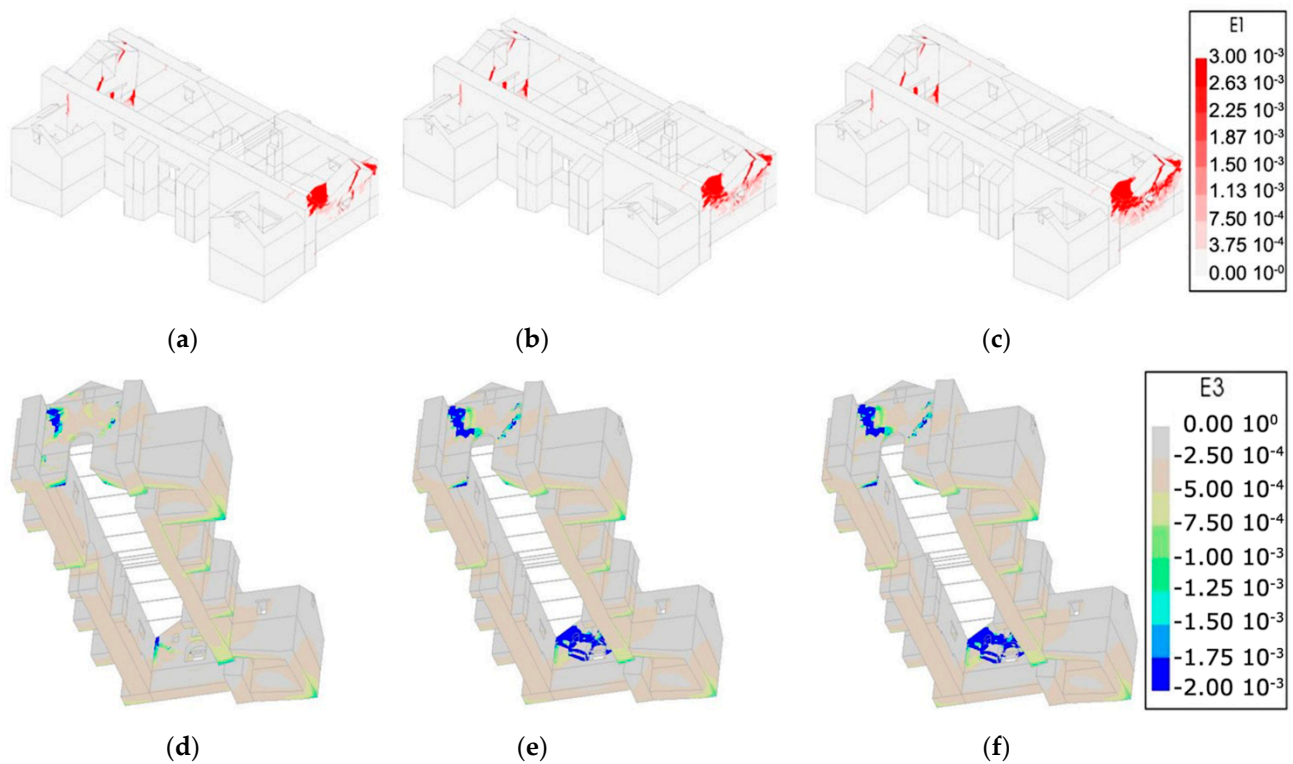


**Figure 23.** Distribution maximum principal strain in +XX direction at the ultimate stage of (a) NTC 2018, (b) KADET 2021 and (c) ASCE41-13. Distribution minimum principal strain in +XX direction at the ultimate stage of (d) NTC 2018, (e) KADET 2021 and (f) ASCE41-13.

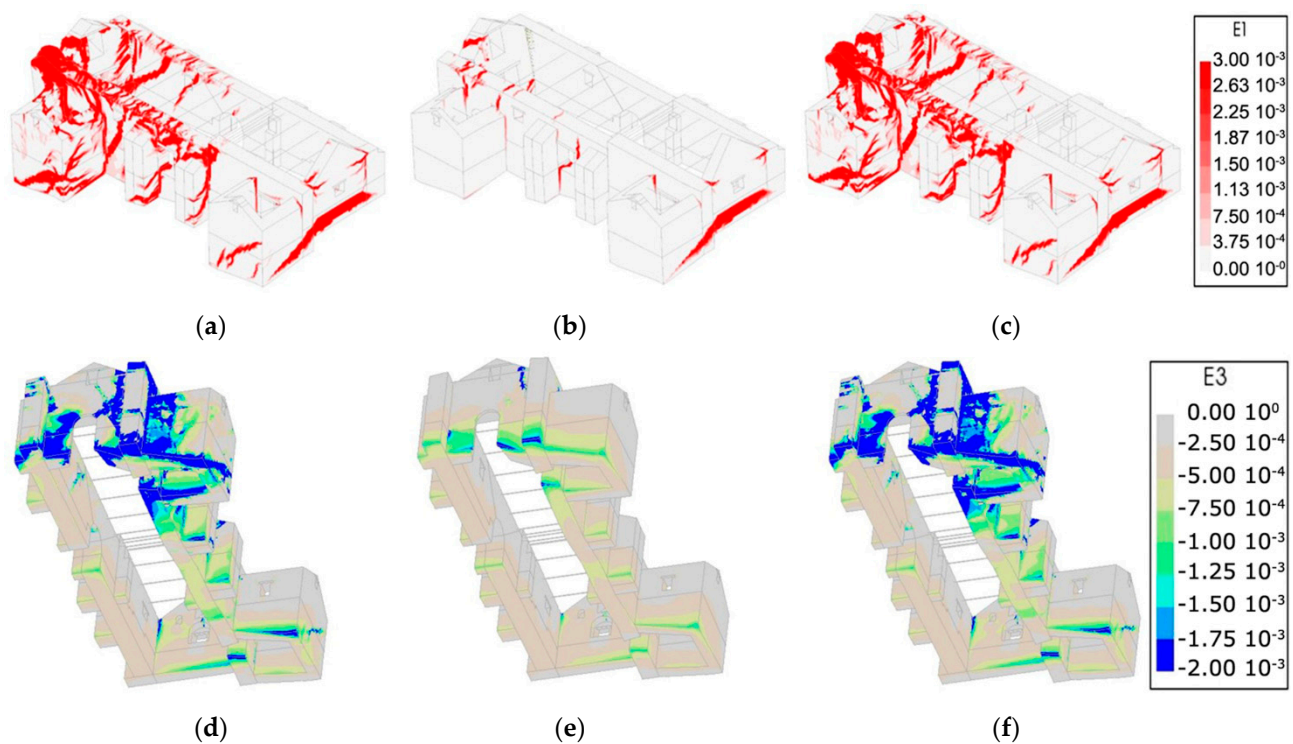


**Figure 24.** Distribution maximum principal strain in -XX direction at the ultimate stage of (a) NTC 2018, (b) KADET 2021 and (c) ASCE41-13. Distribution minimum principal strain in -XX direction at the ultimate stage of (d) NTC 2018, (e) KADET 2021 and (f) ASCE41-13.

After determining the ultimate displacements, the capacity curves obtained from the analysis of the MDOF system were converted into the equivalent SDOF. The SDOF system's equivalent mass ( $m^*$ ) was calculated from Equation (2) as a function of the normalized modal displacements ( $\Phi_i$ ) of the individual nodal masses ( $m_i$ ) using a postulated mode shape in each direction. Mode shapes were selected based on their correspondence to the out-of-plane translational deformations observed at the ultimate displacement stage. Displacements were normalized so that  $\Phi_n = 1$  for the control node. The force ( $F^*$ ) and displacement ( $D^*$ ) of the equivalent SDOF system are related to the base shear force ( $F_b$ ) and control nodal displacement ( $D_n$ ) of the real system by applying the transformation factor ( $\Gamma$ ), as shown in Equations (3)–(5) [22].

$$m^* = \sum m_i \Phi_i^2 \quad (2)$$

$$F^* = \frac{F_b}{\Gamma} \quad (3)$$

$$D^* = \frac{D_n}{\Gamma} \quad (4)$$

$$\Gamma = \frac{m^*}{\sum m_i \Phi_i^2} \quad (5)$$

Bilinear idealization of the SDOF capacity curves was performed as per the recommendations in NTC 2018 [22], but adopting the ultimate displacements computed according to ASCE41-13 [40]. The shear force ( $F_y^*$ ) and displacement ( $D_y^*$ ) at yield were graphically estimated based on the criterion of equal areas under the real and idealized curves, up to the ultimate displacement ( $D_m^*$ ) previously determined. Using the formula  $S = F^*/m^*$ , each idealized bilinear capacity curve was transformed into an acceleration–displacement graph. The elastic period ( $T^*$ ) of the SDOF system is calculated by [22]:

$$T^* = 2\pi \sqrt{\frac{m^* D_y^*}{F_y^*}} \quad (6)$$

The obtained period was used to calculate the  $S_e(T^*)$  ordinate of the elastic acceleration response spectrum, assuming a 5% damping ratio [43]. It was found that in all seismic scenarios, the structure falls within the short-period range and exhibits a nonlinear response because  $T^* \leq T_c$  and  $F_y^*/m^* < S_e(T^*)$ . Consequently, the SDOF system's target displacement ( $D_t^*$ ) could be derived from Equations (7) and (8).

$$D_{et}^* = S_e(T^*) \left[ \frac{T^*}{2\pi} \right]^2 \quad (7)$$

$$D_t^* = \frac{D_{et}^*}{q_u} (1 + (q_u - 1) \frac{T_c}{T^*}) \quad (8)$$

Here,  $q_u = S_e(T^*)m^*/F_y^*$  is the ratio of the acceleration in a structure with unlimited elastic behavior to a structure with finite strength. Three limit states of performance were considered [44]: Damage Limitation (DL), Significant Damage (SD) and Near Collapse (NC), which translate to a probability of exceedance of 20%, 10% and 2%, respectively, over a period of 50 years and a respective PGA of 0.15 g, 0.25 g and 0.43 g. The idealized SDOF capacity curves are plotted against the response spectra of the three different performance levels [44] in Figures 25–28 for each of the four directions considered in the pushover analysis. The figures also show the damage distribution upon achieving the target displacement at each performance level. Table 9 reports the calculated target displacement values for the MDOF structure.

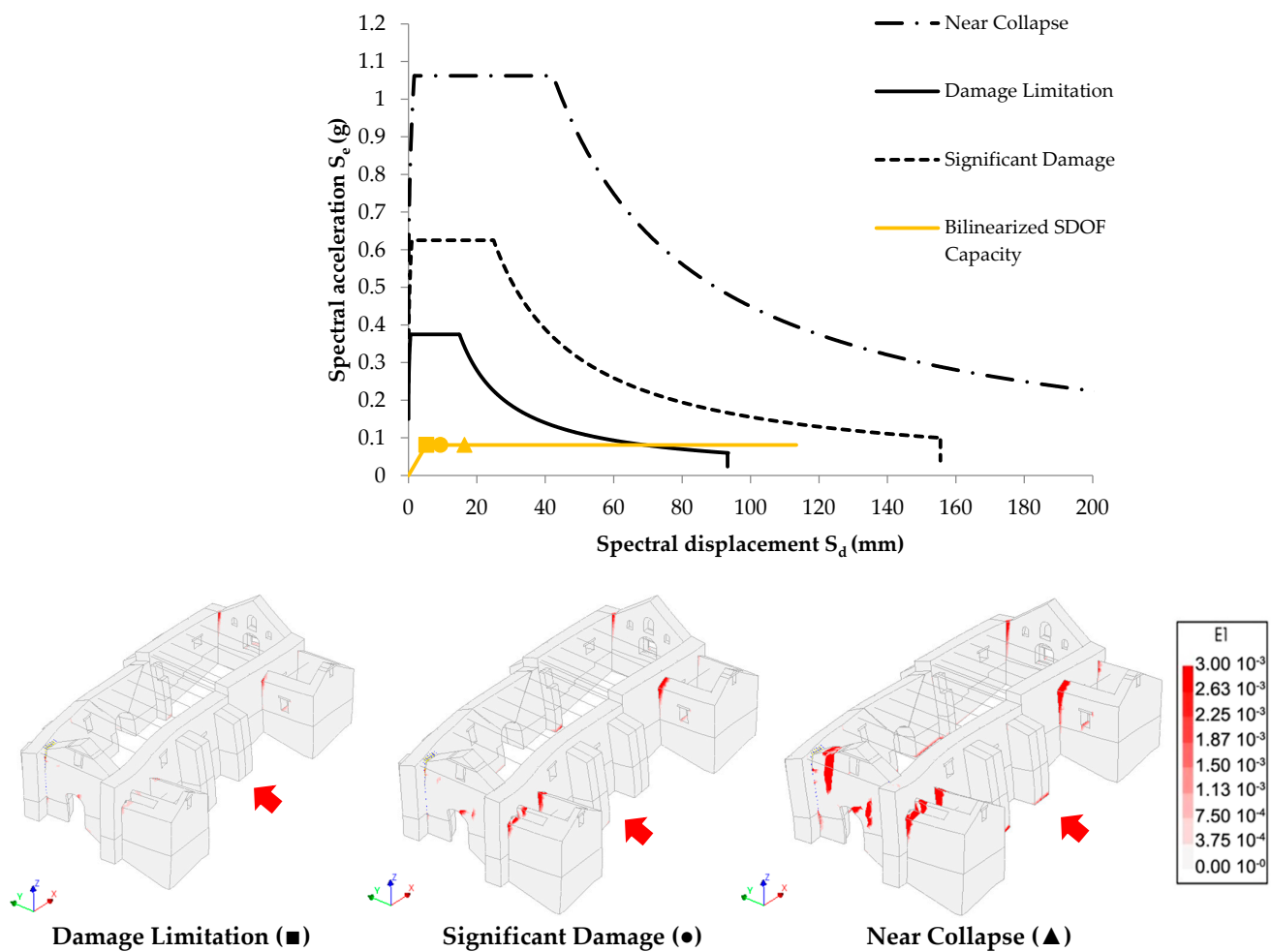


**Figure 25.** Damage Limitation (solid black line), Significant Damage (dotted black line) and Near Collapse (dash-dot black line) elastic demand spectra and bilinearized SDOF capacity diagrams indicating the target displacements (■, ●, ▲) in the +YY direction. The distribution of maximum principal plastic strains corresponding to the attainment of the target displacement at each performance level is shown in the contour diagrams.

It can be seen that in all directions, the DL state is located at the yield point of the idealized capacity curve, while the SD state is placed right after the post peak. By comparing the damage distributions at the NC limit state with those of the ultimate analysis step of the MDOF system, all the main cracks responsible for the ultimate failure mechanism have already been formed, even though the damage areas are not fully progressed. In the  $-XX$  direction, and at the NC state, the west façade exhibits overturning after the formation of horizontal cracking along its base. At the same time, diagonal cracking occurs on the front façade wall and spreads along the entire length of connected masonry sections. In the  $+XX$  direction, the cracks separating the segment of the west and east façade that overturn under lateral loading are practically formed at the DL limit state and progressively evolve until the NC target displacement is attained. Considering the  $+YY$  and  $-YY$  directions, the tensile damage along the base supports of the buttresses occurs at the DL state. Tensile damage vastly progresses during the SD and NC limit states at the side parts of the nave and altar walls. Even though the imposed deformation demands do not exceed the projected ultimate displacement capacity of the MDOF system, both the SD and NC limit state conditions exceed the yield points of the idealized pushover curve and, hence, the structure is expected to exhibit a nonlinear response, with projected damage. Yet, the response under an earthquake for a 10% probability of exceedance within 50 years return period is close to the yield point and is considered sufficient, with limited, repairable structural damage.

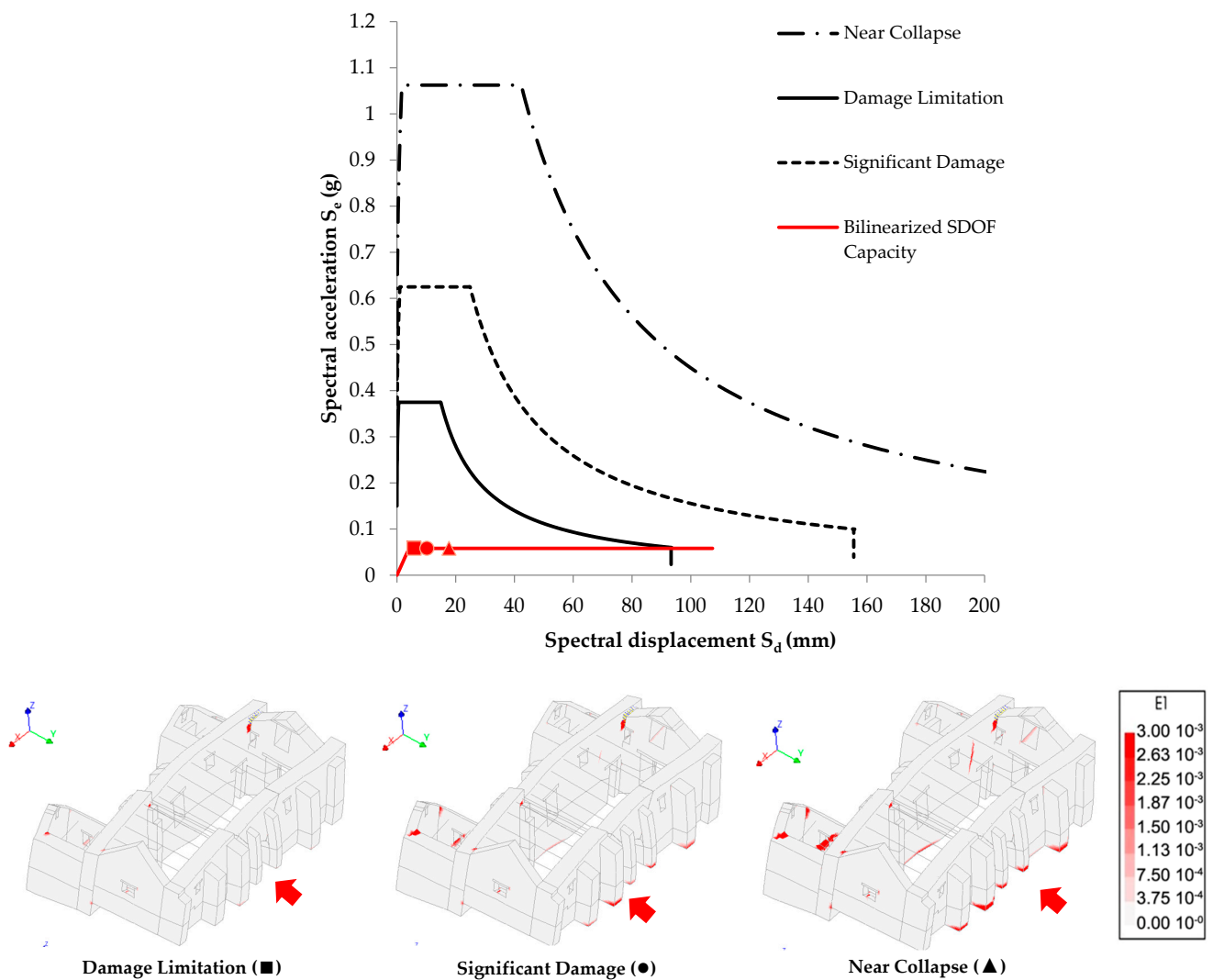


**Figure 26.** Damage Limitation (solid black line), Significant Damage (dotted black line) and Near Collapse (dash-dot black line) elastic demand spectra and bilinearized SDOF capacity diagrams indicating the target displacements (■, ●, ▲) in the  $-YY$  direction. The distribution of maximum principal plastic strains corresponding to the attainment of the target displacement at each performance level is shown in the contour diagrams.

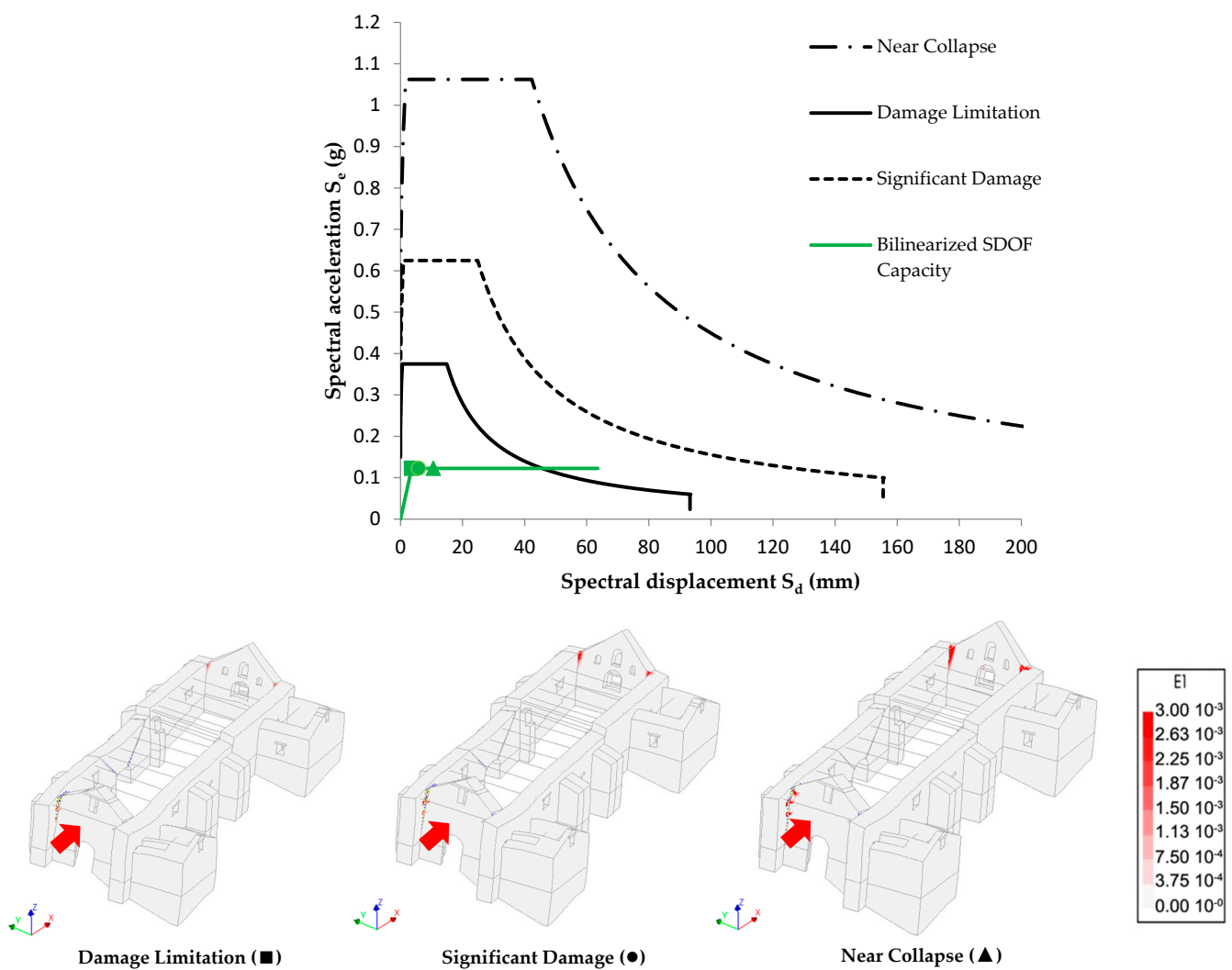


**Figure 27.** Damage Limitation (solid black line), Significant Damage (dotted black line) and Near Collapse (dash-dot black line) elastic demand spectra and bilinearized SDOF capacity diagrams indicating the target displacements (■, ●, ▲) in the +XX direction. The distribution of maximum principal plastic strains corresponding to the attainment of the target displacement at each performance level is shown in the contour diagrams.

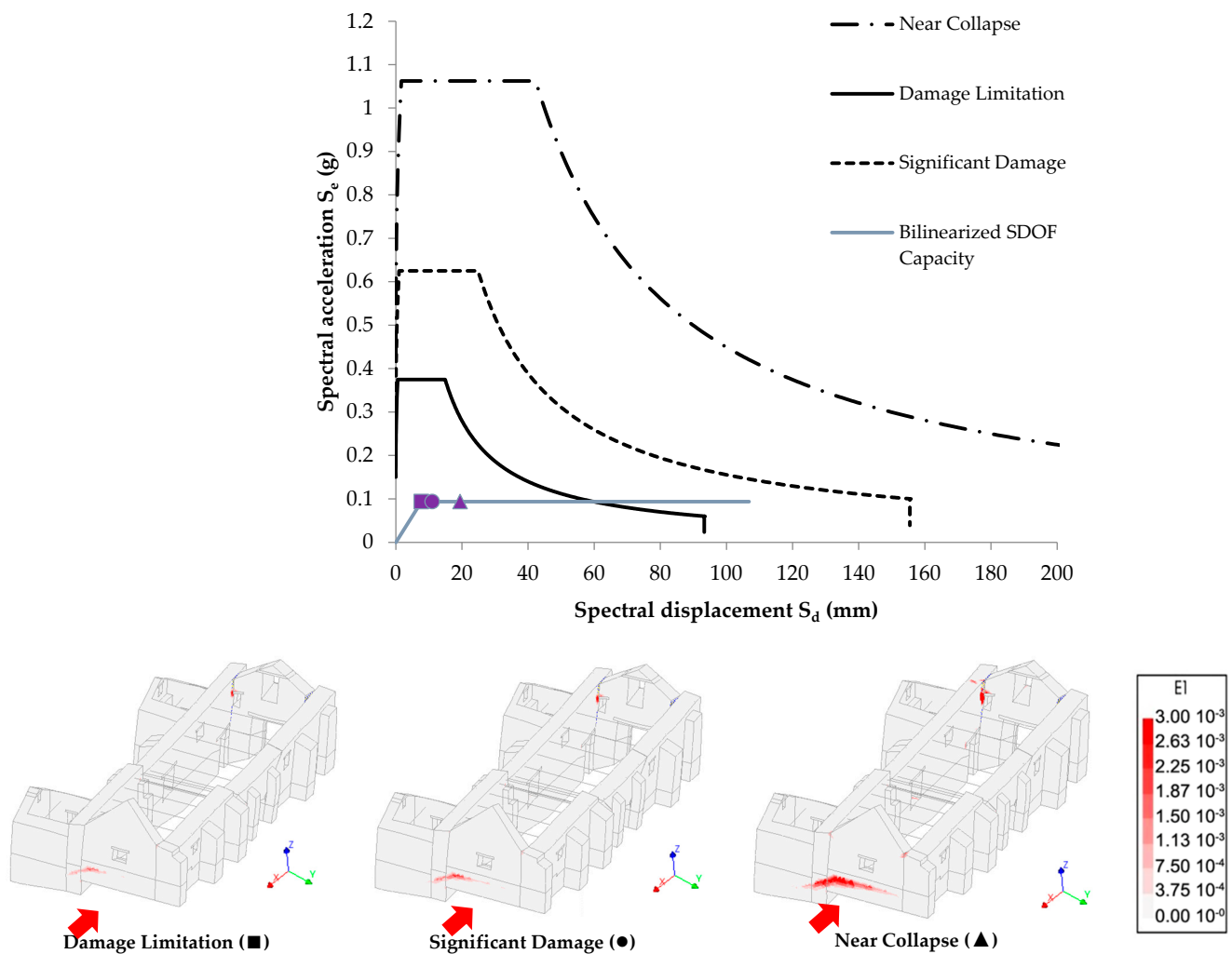


**Figure 28.** Damage Limitation (solid black line), Significant Damage (dotted black line) and Near Collapse (dash-dot black line) elastic demand spectra and bilinearized SDOF capacity diagrams indicating the target displacements (■, ●, ▲) in the  $-XX$  direction. The distribution of maximum principal plastic strains corresponding to the attainment of the target displacement at each performance level is shown in the contour diagrams.

**Table 9.** Data used to obtain target displacement of MDOF system for different performance limit states.

Direction	Assumed Shape	Equivalent Mass (tons)— $m^*$	Transformation Factor— $G$	Period of Idealized SDOF System— $T^*$ (s)	Target Displacement of MDOF System— $D_t$ (mm)		
					DL	SD	NC
+YY	Mode 1	419.41	2.382	0.162	12.6	22.2	39.1
−YY	Mode 5	624.92	2.514	0.173	14.8	25.6	44.6
+XX	Mode 4	184.98	4.249	0.109	13.3	24.8	45.1
−XX	Mode 7	446.29	2.595	0.194	16.1	26.6	50.5

## 8. Conclusions

This study aimed to demonstrate a comprehensive approach for the structural appraisal of strengthening interventions to historic buildings, through the analysis of the Kuñotambo Church in Peru. Retrofitting for the case study monument was validated and later inspected by the University of Minho between 2016–2019. In situ inspections, condition mapping, sonic tests and dynamic identification tests proved highly effective

for advancing the knowledge on material properties, deformation, boundary conditions and connectivity between parts. Sonic tests helped determine the stiffness characteristics of the materials present, but also allowed a comparison between new and older masonry parts. Modal updating proved to be particularly useful for the validation of FE models. The introduction of cracks and discontinuities, recorded during field investigations, resulted in an almost perfect match between experimental and numerical modes.

The pushover method with mass-proportional loading was employed for the seismic analysis of the retrofitted church. The damage patterns and capacity estimations obtained from the analyses were consistent with previous works [4] and showed an acceptable performance after strengthening. Failure modes of the retrofitted church were shown to be mostly the result of out-of-plane movements. However, a better distribution of deformations was noted after strengthening as a result of the improved connectivity among repaired sections and the addition of lateral timber bracing elements. Thus, the global response was found to be characterized by mixed failure modes involving out-of-plane rotations and diagonal or vertical in-plane shear cracks.

The application of the performance-based assessment process prescribed in current seismic codes was examined. Target displacements corresponding to three different limit states of performance were determined using a SDOF transformation method adapted to the case of masonry structures modelled with continuum FE meshes. For the SD limit state, the response of the structure was found to be sufficient, but nonlinear, with minor repairable damage. More widespread damage is predicted for the NC limit state, yet the damage is still considered repairable.

The general concluding aspects of this paper are summarized as followed:

- In the process of modal updating, using a proper reference model is necessary to obtain good results for the final model. In this study, a model with interfaces (replicating existing cracks) in different parts was required to obtain a good validation and match with the dynamic properties measured.
- Automatic model updating is a fast tool to obtain results, but realistic bounds of material properties, together with carefully selected updating parameters and representative modes are needed. Engineering educated guesses remain important and the process does not replace an experience modeler.
- To obtain the ultimate out-of-plane displacement of strengthened models, recommendations from three building codes—ASCE41-13, KADET 2021 and NTC 2018—can be used, with engineering judgment needed to select which code is more adequate for monumental masonry buildings. Here, ASCE41-13 was selected, being more representative in terms of corresponding damage.
- A displacement-based approach was hereby adopted for the equivalent bilinearization of nonlinear system response. This proved to be an efficient tool for validating the damage conditions in masonry buildings and can be useful in the context of interpreting the results obtained from nonlinear static and dynamic analyses. Yet, the full progression of damage that can be found in later stages of the capacity curves should be also accounted for retrofitting design procedures, especially with respect to the location of damage in crushing zones and fully formed shear cracks.

**Author Contributions:** Writing – original draft, S.S.A. and G.K.; visualization, S.S.A. and G.K.; methodology, S.S.A., G.K., N.M., R.I. and P.B.L.; formal analysis, S.S.A., G.K. and N.M.; data curation, S.S.A., G.K. and N.M.; investigation, G.K. and R.I.; resources, G.K., N.M. and R.I.; validation, G.K., N.M., R.I. and P.B.L.; software, N.M.; supervision, P.B.L.; project administration, P.B.L.; conceptualization, P.B.L.; writing – review & editing, G.K., N.M., R.I. and P.B.L. All authors have read and agreed to the published version of the manuscript.

**Funding:** Partial funding by Getty Conservation Institute – Seismic Retrofitting Project.

**Institutional Review Board Statement:** Not applicable.

**Informed Consent Statement:** Not applicable.



**Data Availability Statement:** Data will be available upon a reasonable request to the authors.

**Conflicts of Interest:** The authors declare no conflict of interest.

## References

1. Houben, H.; Guillaud, H. *Earth Construction: A Comprehensive Guide*; Intermediate Technology Publications: London, UK, 2008.
2. Minke, G. *Building with Earth: Design and Technology of a Sustainable Architecture*; Birkhauser for Architecture: Basel, Switzerland, 2006.
3. Mirjalili, A.; Eslami, A.; Morshed, R. Experimental investigation into the effect of vertical loading on in-plane cyclic behavior of adobe walls. *Constr. Build. Mater.* **2020**, *264*. [[CrossRef](#)]
4. Karanikoloudis, G.; Lourenço, P.B. Structural assessment and seismic vulnerability of earthen historic structures. Application of sophisticated numerical and simple analytical models. *Eng. Struct.* **2018**, *160*, 488–509. [[CrossRef](#)]
5. Lourenco, P.B.; Gaetani, A. *Finite Element Analysis for Building Assessment, Advanced Use and Practical Recommendations*; Routledge, Taylor and Francis Group: London, UK, 2022.
6. Cancino, C. *Damage Assessment of Historic Earthen Buildings after the 15 August 2007 Pisco, Perú Earthquake*; Getty Conservation Institute: Los Angeles, CA, USA, 2011. Available online: [http://hdl.handle.net/10020/gci\\_pubs/damage\\_assessment](http://hdl.handle.net/10020/gci_pubs/damage_assessment) (accessed on 25 August 2022).
7. Varum, H.; Tarque, N.; Silveira, D.; Camata, G.; Lobo, B.; Blondet, M.; Figueiredo, A.; Rafi, M.M.; Oliveira, C.; Costa, A. *Structural Behaviour and Retrofitting of Adobe Masonry Buildings*; Springer: Berlin/Heidelberg, Germany, 2014; pp. 37–75. [[CrossRef](#)]
8. Blondet, M.; Vargas, J.; Tarque, N. Observed behavior of earthen structures during the Pisco (Peru) earthquake of 15 August 2007. In Proceedings of the 14th World Conference on Earthquake Engineering, Beijing, China., 12–17 October 2008.
9. Lourenço, P.B.; Ciocci, M.P.; Greco, F.; Karanikoloudis, G.; Cancino, C.; Torrealva, D.; Wong, K. Traditional techniques for the rehabilitation and protection of historic earthen structures: The seismic retrofitting project. *Int. J. Archit. Herit.* **2019**, *13*, 15–32. [[CrossRef](#)]
10. Mentese, V.G.; Celik, O.C. 3D FE Modeling of Multi-Span Stone Masonry Arch Bridges for the Assessment of Load Carrying Capacity: The Case of Justinian’s Bridge. In Proceedings of the 12th International conference on Structural Analysis of Historical Constructions (SAHC 2021), Barcelona, Spain, 29 September–1 October 2021.
11. Celik, O.C.; Sesigur, H.; Cili, F. Seismic Evaluation and Retrofit of A 16th Century Historic Brick Masonry Dome in Istanbul using Combined Steel Rings and CFRP Sheets. Proceedings of 14th World Conference on Earthquake Engineering, Beijing, China, 12–17 October 2008.
12. Sesigur, H.; Celik, O.C.; Cili, F. Repair and Strengthening of Ancient Structures in Seismic Areas. In Proceedings of the First European Conference on Earthquake Engineering and Seismology, Geneva, Switzerland, 3–8 September 2006.
13. Cancino, C.; Lardinois, S.; D’Ayala, D.; Ferreira, C.; Dávila, D.; Meléndez, E. *Seismic Retrofitting Project: Assessment of Prototype Buildings*; Getty Conservation Institute: Los Angeles, CA, USA, 2013. Available online: [http://hdl.handle.net/10020/gci\\_pubs/assess\\_prototype](http://hdl.handle.net/10020/gci_pubs/assess_prototype) (accessed on 25 August 2022).
14. NTE E.030; Technical Standard of building E.030 Earthquake-Resistant Design. Ministry of Housing, Construction and Sanitation: Lima, Peru, 2016.
15. Vintzileou, E. Effect of Timber Ties on the Behavior of Historic Masonry. *J. Struct. Eng.* **2008**, *134*, 961–972. [[CrossRef](#)]
16. *Seismic Retrofitting Project*; Getty Conservation Institute: Los Angeles, CA, USA, 2017. Available online: [https://www.getty.edu/conservation/our\\_projects/field\\_projects/seismic/case\\_study\\_kunotambo.html](https://www.getty.edu/conservation/our_projects/field_projects/seismic/case_study_kunotambo.html) (accessed on 25 August 2022).
17. AIC. *AIC Code of Ethics and Guidelines for Practice*; American Institute for Conservation of Historic and Artistic Works: Washington, DC, USA, 1994.
18. Ramos, L. Damage Identification on Masonry Structures Based on Vibration Signatures. Ph.D. Thesis, University of Minho, Guimaraes, Portugal, 2007.
19. *ARTEMIS Extractor Pro User Manual*; Structural Vibration Solutions A/S: Aalborg, Denmark, 2006. Available online: <https://www.svibs.com> (accessed on 25 August 2022).
20. Karanikoloudis, G.; Lourenço, P.B. *Experimental In Situ Testing and Visual Inspection of a Retrofitted Adobe Historic Structure, within the Getty Seismic Retrofitting Project*; The Church of Kuñotambo: Cusco, Peru; Guimaraes, Portugal, 2020.
21. Sánchez, A.; Varum, H.; Martins, T.; Fernández, J. Mechanical properties of adobe masonry for the rehabilitation of buildings. *Constr. Build. Mater.* **2022**, *333*, 127330. [[CrossRef](#)]
22. NTC. *Istruzioni per l’applicazione dell’«Aggiornamento delle “Norme tecniche per le costruzioni”» di cui al decreto ministeriale 17 gennaio 2018*; Ministero delle infrastrutture e dei trasporti: Roma, Italy, 2019. (In Italian)
23. Lourenço, P.B. *Computational Strategies for Masonry Structures*; Delft University of Technology: Delft, The Netherlands, 1996.
24. Illampas, R.; Charmpis, D.C.; Ioannou, I. Laboratory testing and finite element simulation of the structural response of an adobe masonry building under horizontal loading. *Eng. Struct.* **2014**, *80*, 362–376. [[CrossRef](#)]
25. *DIANA User’s Manual*; DIANA FEA bv: Delft, The Netherlands, 2020. Available online: <https://dianafea.com> (accessed on 25 August 2022).
26. Kuklik, P.; Hansen, A.S. *Handbook 2—Design of Timber Structures According to EC 5*; Leonardo da Vinci Pilot Project CZ/06/B/F/PP/168007: Prague, Czech Republic, 2008.

27. Sousa, H.; Sørensen, J.D.; Kirkegaard, P.H. *Reliability Analysis of Timber Structures through NDT: Short Term Scientific Mission, COST E55 Action*; Aalborg University: Aalborg, Denmark, 2010.
28. JCSS. *Probabilistic Model Code Part 3: Resistance Models, 3.5 Properties of Timber*; Joint Committee of structural safety: Zürich, Switzerland, 2006.
29. *RNE E.10*; Technical Norm for Design of Timber Elements for Structural Use. Ministry of Housing, Construction and Sanitation: Lima, Peru, 2006.
30. Torrealva, D.; Erika, V.; Tim, M. *Seismic Retrofitting Project: Testing of Materials and Building Components of Historic Adobe Buildings in Peru*; Getty Conservation Institute: Los Angeles, CA, USA, 2018; Available online: [https://hdl.handle.net/10020/gci\\_pubs/testing\\_materials](https://hdl.handle.net/10020/gci_pubs/testing_materials) (accessed on 25 August 2022).
31. Carvalho, J.; Datta, B.N.; Gupta, A.; Lagadapati, M. A direct method for model updating with incomplete measured data and without spurious modes. *Mech. Syst. Signal Process.* **2007**, *21*, 2715–2731. [[CrossRef](#)]
32. Yang, Y.B.; Chen, Y.J. A new direct method for updating structural models based on measured modal data. *Eng. Struct.* **2009**, *31*, 32–42. [[CrossRef](#)]
33. Teughels, A.; de Roeck, G.; Suykens, J.A.K. Global optimization by coupled local minimizers and its application to FE model updating. *Comput. Struct.* **2003**, *81*, 2337–2351. [[CrossRef](#)]
34. Ribeiro, D.; Calçada, R.; Delgado, R.; Brehm, M.; Zabel, V. Finite element model updating of a bowstring-arch railway bridge based on experimental modal parameters. *Eng. Struct.* **2012**, *40*, 413–435. [[CrossRef](#)]
35. Douglas, B.M.; Reid, W.H. Dynamic Tests and System Identification of Bridges. *J. Struct. Div.* **1982**, *108*, 2295–2312. [[CrossRef](#)]
36. Lourenço, P.B.; Mendes, N.; Ramos, L.F.; Oliveira, D.V. Analysis of Masonry Structures Without Box Behavior. *Int. J. Archit. Herit.* **2011**, *5*, 369–382. [[CrossRef](#)]
37. Mendes, N. *Seismic Assessment of Ancient Masonry Buildings: Shaking Table Tests and Numerical Analysis*. PhD Thesis, University of Minho, Guimaraes, Portugal, 2012.
38. Kalkbrenner, P.; Pelà, L.; Sandoval, C. Multi directional pushover analysis of irregular masonry buildings without box behavior. *Eng. Struct.* **2019**, *201*, 109534. [[CrossRef](#)]
39. Illampas, R.; Ioannou, I.; Lourenço, P.B. Seismic appraisal of heritage ruins: The case study of the St. Mary of Carmel church in Cyprus. *Eng. Struct.* **2020**, *224*, 111209. [[CrossRef](#)]
40. *ASCE/SEI 41-13*; Seismic Evaluation and Retrofit of Existing Buildings. American Society of Civil Engineers: Reston, VA, USA, 2014.
41. KADET. *Normative for Assessment and Structural Interventions in Masonry (Under Review)*; Greek Ministry of Infrastructure, Transport and Networks: Athens, Greece, 2021. (In Greek)
42. Karantoni, F.V.; Papadopoulos, M.L.; Pantazopoulou, S.J. Simple Seismic Assessment of Traditional Unreinforced Masonry Buildings. *Int. J. Archit. Herit.* **2016**, *10*, 1055–1077. [[CrossRef](#)]
43. Chopra, A. *Dynamics of Structures: Theory and Applications to Earthquake Engineering*, 3rd ed.; Prentice Hall: Hoboken, NJ, USA, 2001.
44. *EN 1998-1*; Eurocode 8: Design of Structures for Earthquake Resistance—Part 1: General Rules, Seismic Actions and Rules for Buildings. The European Union: Brussels, Belgium, 2004.